Corresponding Author: Dr. fangnao xiao, Ph.D.

Corresponding Author's Institution: Univ. Bourgogne Franche-Comté, FEMTO-
ST Institute, CNRS/UFC/ENSMM/UTBM

First Author: fangnao xiao, Ph.D.

Order of Authors: fangnao xiao, Ph.D.; Thierry Barriere; Gang Cheng;
Qiang Miao; Shizhong wei; Shiwei zuo; liujie xu

Abstract: Doped hexagonal ammonium tungsten bronze [(NH4)x·WO3, HATB]
powder used for elaborating oxide particle dispersion-strengthened
tungsten alloys has received much more attention due to its high activity
and special opened-tunneling structures. In this article, the in situ
nanosized Zr(Y)O2 particles uniformly distributed in the tungsten alloy
was successfully prepared through synthesizing doped α-HATB powder and
spark plasma sintering process. The processing route involves a
molecular-level liquid-liquid doping technique that causes a large number
of nanosized particles within tungsten grains. The synthesis mechanism of
α-HATB and phase evolution were detailedly investigated. Over 75 % of W-
Zr(Y)O2 powders particles are less than 3 μm. The determined Sw values
(5.7), coefficient of uniformity Cu (2.3) of the W-0.5% Zr(Y)O2 doped
tungsten are 5.7 and 2.3, respectively, both indicating the narrower size
distribution. The average size of Zr(Y)O2 particles in prepared W alloy
are about 250 nm under SEM observation. Through milling of these powders,
the particles in W-0.5%Zr(Y)O2 alloy and 92.5W-4.9Ni-2.1Fe-0.5%ZrO2 can
further decrease to less than 100 nm in size, which are 8-10 times
smaller than those in the state-of-the-art review.

Research on preparation process for the in situ nanosized $Zr(Y)O_2$ particles dispersion-strengthened tungsten alloy through synthesizing doped hexagonal $(NH_4)_{0.33}\cdot WO_3$

Fangnao Xiao [a, c], Thierry Barriere [a], Gang Cheng [b], Qiang Miao [c]*, Shizhong Wei [d]*, Shiwei Zuo [c], Zhimin Huang [e], Liujie Xu [d]*

[a] Univ. Bourgogne Franche-Comté, FEMTO-ST Institute, CNRS/UFC/ENSMM/UTBM, Department of Applied Mechanics, 25000 Besançon, France

[b] INSA CVL, Univ. Tours, Univ. Orléans, LaMé, 3 rue de la Chocolaterie, BP 3410, 41034 Blois Cedex, France

[c] College of Material Science and Technology, Nanjing University of Aeronautics and Astronautics, 29 Yudao Street, Nanjing 210000, China

[d] National Joint Engineering Research Center for abrasion control and molding of metal materials, Henan University of Science and Technology, Luoyang 471003, China

[e] China National R&D Center for Tungsten Technolog，Xiamen Tungsten Corporation, Ltd.，Xiamen， Fujian 361000， China

*Corresponding author

Tel.:+86-379-64270020

E-mail addresses: miaoqiang@nuaa.edu.cn (Qiang Miao)

wsz@haust.edu.cn (Shizhong Wei)

xlj@haust.edu.cn (Liujie Xu)

Abstract

In this article, the in situ nanosized Zr(Y)O$_2$ particles uniformly distributed in the tungsten alloy was successfully prepared through synthesizing doped α-HATB powder and spark plasma sintering process. The processing route involves a molecular-level liquid–liquid doping technique that causes a large number of nanosized particles within tungsten grains. The synthesis mechanism of α-HATB and phase evolution were detailedly investigated. Over 75 % of W-Zr(Y)O$_2$ powders particles are less than 3 μm. The determined S$_w$ values (5.7), coefficient of uniformity C$_u$ (2.3) of the W-0.5% Zr(Y)O$_2$ doped tungsten are 5.7 and 2.3, respectively, both indicating the narrower size distribution. The average size of Zr(Y)O$_2$ particles in prepared W alloy are about 250 nm under SEM observation. Through milling of these powders, the particles in W-0.5%Zr(Y)O$_2$ alloy and 92.25W-4.9Ni-2.1Fe-0.75ZrO$_2$ can further decrease to less than 100 nm in size, which are 8-10 times smaller than those in the state-of-the-art review.

Keywords: Hydrothermal process; Ammonium tungsten bronze; In situ oxide dispersion strengthening; Zirconia; Spark plasma sintering.

Nomenclature

C$_u$	Coefficient of uniformity
d$_{50}$	Particle sizes at 50% of the cumulative volume percentage
F$_{ag}$	Agglomeration factor
S$_w$	Distribution slope parameter
Ψ	Span value
α-HATB	Hexagonal ammonium tungsten bronze (NH$_4$)$_{0.33}$·WO$_3$
β-HATB	(NH$_4$)$_{0.42}$WO$_3$ / (NH$_4$)$_{0.06}$WO$_3$·(H$_2$O)$_{0.11}$
AMT	Ammonium metatungstate
APT	Ammonium paratungstate
BSE	Backscattered electron

CVT	Chemical vapor transport
DSC	Differential Scanning Calorimeter
EDS	Electron dispersive spectroscopy
FWHM	Full width at half maxima
HATB	Hexagonal ammonium tungsten bronze, $(NH_4)_x \cdot WO_3$
HIP	Hot isostatic pressing
HR-TEM	High-resolution transmission electron microscopy
L-L	Liquid-liquid
L-S	Liquid-solid
ODS-W	Oxide particles dispersion-strengthened tungsten
PSD	Particle-size distribution
SAEDP	Selected area electron diffraction pattern
SEM	Scanning electron microscope
SSA	Specific surface area
SPS	Spark plasma sintering
S-S	Solid-solid
TGA	Thermogravimetric analysis
VD	Sintering process in vertical direction
XRD	X-ray diffraction

1. Introduction

Over the past years, oxide particles (such as ZrO_2, La_2O_3, and Y_2O_3) dispersion-strengthened tungsten alloys (ODS-W) are used as plasma facing material in future fusion reactors owing to their high melting point, high-temperature antiwear high-temperature strength and high-thermal conductivity [1-4]. With the development of increasingly accurate and netshape powder metallurgy manufacturing processing, the mechanical properties of tungsten alloys depend on the quality of tungsten powder to some extent [5-10]. Mazher Ahmed Yar et al. [11, 12] reported the W-Y_2O_3 and La_2O_3 powder through solid-liquid doping method using ammonium paratungstate (APT) as materials. The doped powders consisted of significant particle aggregates, resulting in heterogeneous distribution of oxide particles. Belgacem Mamen et al. [13] revealed that particle size of powders affected the densification behaviour and sintering stress of tungsten specimens during solid state sintering.

To improve the quality of tungsten powders for preparing high-performance tungsten products, over the past several years, the liquid-liquid (L-L) doping techniques, particularly spray drying [14-19] and evaporation-precipitation/sol-gel process [20-23], were introduced to synthesize doped tungsten powders. On the one hand, it can avoid the introduction of detrimental contaminants during the mixing process of doping phase and tungsten powder. On the other hand, it can lead to the doping phase evenly distributed in tungsten powders through the molecular-level mixing. However, the prepared doped tungsten powders also exhibit high degree of agglomeration, such as W-Y_2O_3 powders [15, 21], W-Re powders [16], W-Sc_2O_3 powders [17] and W-As powders [23].

A large number of studies have shown that the physical and chemical characteristics of the precursor powder, the phase evolution process and the evolution of mechanisms affected the resultant reduced powders [24-30]. Hu Yazhou et al. and Hong Seong-Hyeon et al. [15, 26] synthesized the spherical doped precursor W-Y_2O_3 and W-Cu powders through spray drying method, respectively. The resultant doped tungsten powders were composed of solid agglomerates. Yoon Eui-Sik et al. [27]

reported the H_2 reduction behavior of powders can be significantly affected by the microstructure and composition of tungsten powders. Wu Chonghu et al. [28] pointed out that tungsten blue oxide ($WO_{2.72}$, $WO_{2.90}$, $W_{20}O_{58}$ or $(NH_4)_x \cdot WO_3$) would be an ideal materials for preparing ultrafine tungsten alloy powders through dry hydrogen reduction. It was reported that the physical properties of tungsten powder would be determined by different transition sequences from tungsten blue oxide to W to some extent, which depend on the operating conditions (reduction temperature, holding time and H_2O partial pressure) [29-30].

Among tungsten blue oxide, the metastable phases of hexagonal ammonium tungsten bronze $(NH_4)_x \cdot WO_3$ (HATB) have attracted a lot of attention during the last decades [31, 32]. Due to their special channel structures, large specific surface area and high-activity, they are used in catalytic detectors, color development devices and gas sensors [31-33]. They are also preferred materials for producing tungsten filaments in the lighting, extremely hard and refractory metal industry [32, 34, 35].

According to the above analysis mentioned, the doped HATB with high-dispersity synthesized through liquid-liquid doping technique would be expected to produce high-quality doped tungsten powders and alloys. In this work, the nanosized $Zr(Y)O_2$ particles uniformly distributed in the tungsten alloys are fabricated through the novel composite hydrothermal method and spark plasma sintering process. Composite hydrothermal method and reaction mechanism for preparing highly dispersed doped α-HATB is deeply investigated in detail. Through optimized hydrogen reduction process of doped α-HATB, the fine doped tungsten powders particles are obtained and have a narrower size distribution. Moreover, the phase composition and morphology evolution are investigated. After sintering, the nanosized $Zr(Y)O_2$ particles uniformly distributed in the developed tungsten alloy are realized, which are considerably smaller than those in the state-of-the-art review. Our approach can readily be adapted to manufactured nanosized $Zr(Y)O_2$ particles dispersion-strengthened W and 92.25W-4.9Ni-2.1Fe-0.75ZrO$_2$ through the proposed liquid-liquid doping and hot isostatic pressing processes.

2. Experimental methods

2.1 Composition of samples

The compositions of doped tungsten powders were listed in Table 1. Five kinds of doped tungsten powders consist of the following types: with 0 wt% $Zr(Y)O_2$, 0.25 wt% $Zr(Y)O_2$, 0.5 wt% $Zr(Y)O_2$, 0.75 wt% $Zr(Y)O_2$ and 5 wt% $Zr(Y)O_2$, respectively. The $H_{5.0}$ sample was used to investigate the composition of doped powder through X-ray diffraction (XRD) analysis.

Table 1 Composition of five kinds of doped tungsten powders.

Samples	W	ZrO_2	Y_2O_3
H_0	100	0	0
$H_{0.25}$	99.718	0.250	0.032
$H_{0.50}$	99.437	0.500	0.063
$H_{0.75}$	99.154	0.750	0.096
$H_{5.0}$	94.370	5.000	0.630

2.2. Preparation of composite powders and alloys

In this research, the $W-Zr(Y)O_2$ powders were synthesized through composite hydrothermal method, which distinguishes from the multiple step hydrothermal method [3, 36, 37]. Firstly, the raw materials, which are commercial $ZrOCl_2 \cdot 8H_2O$ (grade AR), $Y(NO_3)_3 \cdot 6H_2O$ (grade AR) and ammonium metatungstate $(NH_4)_6H_2W_{12}O_{40} \cdot 5H_2O$ (grade AR; AMT), were dissolved in distilled water. Subsequently, a certain amount of $ZrOCl_2 \cdot 8H_2O$ and $Y(NO_3)_3 \cdot 6H_2O$ with [Zr]: [Y] molar ratio of 88:12 were homogeneously mixed by stirring. After that, the mixture solution was dripped into the $(NH_4)_6H_2W_{12}O_{40} \cdot xH_2O$ after stirring for 2 h at room temperature. HNO_3 was used to regulate the pH value of solution to lower than 1.0, forming the resultant solution. Finally, this solution was placed in a stainless-steel autoclave at 120 °C. After the reaction was completed, the autoclave was cooled down to 25 °C. The reaction products were dried and then the doped precursor powders were synthesized. After that, the precursor powder was calcined in air or reduction with hydrogen gas flow rate of 6 l.min^{-1} at different temperature, forming the resultant

doped powders.

The reduced powders were loaded into a graphite mold (grade SS, 1.85g/cm^3) with an inner diameter of 20 mm by manual operation and then were densified using spark plasma sintering (SPS) processes using various sintering conditions in SPS furnace (SPS-20T-10-4) manufactured by Shanghai Chenhua Technology Co., Ltd. The sintering temperatures were adjusted from 1800 °C, 1900 °C, 2000 °C to 2100 °C for 5 minutes under the pressure of 30 MPa by measuring the axial temperature of the sample using infrared double-wave temperature indicator. Samples with approximately 20-mm diameter and 4-mm thickness were realized without defects. For comparative specimens of W-Z(Y)O$_2$ and 92.25W-4.9Ni-2.1Fe-0.75ZrO$_2$ alloys, their original powders were prepared through previous W-Z(Y)O$_2$ powders and highly pure powders of Ni (99.90% purity), Fe(99.90% purity) with particle size of 2.2-2.5 μm and 3.0-6.5 μm, respectively. Then, milling experiments of the W-Zr(Y)O$_2$ and 92.25W-4.9Ni-2.1Fe-0.75ZrO$_2$ powders were carried out in a planetary ball with milling speed of 250 rpm. The milling media is WC ball consisting of 3 mm in diameter with ball to powder ratio of 10:1. The milled W-Z(Y)O$_2$ powder was sintered through the SPS sintering process above. For the 92.25W-4.9Ni-2.1Fe-0.75ZrO$_2$ alloy, the corresponding milled powder was pressed by the cold isostatic pressing process at a pressure of 250 MPa. The green compact was first sintered at 1200 °C for 1.5 h in a hydrogen atmosphere. Then the sintering sample was hot isostatic pressed at 1400 °C under 150 MPa for 2 h using a hot isostatic pressing furnace (RG500) manufactured by China Iron & Steel Research Institute Group, Beijing, China.

2.3 Measurement, experimental procedures and analysis

The reaction process of precursor powders during calcination were studied through Thermogravimetric Analysis (TGA) and Differential Scanning Calorimeter (DSC) using a NETZSCH STA 409 PC/PG thermal analyzer. The composition, crystallite size and full width at half maxima (FWHM) of powders were determined using X-ray diffraction analyses combined with the JADE 5.0 software. The morphology evolution and chemical composition were investigated using a scanning

electron microscope (SEM), electron dispersive spectroscopy (EDS), backscattered electron (BSE) and high-resolution transmission electron microscopy (HR-TEM). Laser diffraction particle size analyzer (Mastersizer-2000) was used to determine the particle-size distribution (PSD) dispersed in ethanol. The specific surface area (SSA) and d_{BET} sizes of doped powders was described as [38]:

The distribution slope parameter, S_w, was calculated from the measured particle size by Eq. (1) [9].

$$S_w = 2.56 / \lg(d_{90}/d_{10}) \tag{1}$$

where the numerator represents the fact that d_{10} and d_{90} are 2.56 standard deviations apart on a Gaussian distribution. The d_{10} and d_{90} are the particle sizes at 10% and 90%, respectively, of the cumulative volume percentage.

The coefficient of uniformity, C_u, is defined by Eq. (2) [10].

$$C_u = d_{60}/d_{10} \tag{2}$$

where d_{60} is the particle sizes at 60% of the cumulative volume percentage.

The span value (Ψ) is calculated using Eq. (3) [39]:

$$\Psi = (d_{90} - d_{10}) / 2\, d_{50} \tag{3}$$

where d_{50} is the particle sizes at 50% of the cumulative volume percentage and is regarded as mean particle size.

The agglomeration factor (F_{ag}) was calculated as shown in Eq. (4) [9]:

$$F_{ag} = d_{50}/d_{BET} \tag{4}$$

where d_{50} is the average diameter of the powders.

The densities of the alloys were determined using by Archimedes' principle. The relative densities were obtained by using the apparent volume mass divided by the theoretical value of 19.18 g/cm^3. Vickers hardness test was made using 200 g indented load and a dwell time of 20 seconds. The average hardness value is performed with 10 randomly selected sample specimens.

3. Results and discussion

3.1 Reaction mechanism of precursor powders

Considering different polytungstate species could exist in aqueous solutions of different acidities (Fig. 1) [18], in order to obtain optimal doping effect, the existence forms and reaction mechanisms of polytungstate ions in aqueous solutions were analyzed.

When $(NH_4)_6H_2W_{12}O_{40} \cdot 5H_2O$ were dissolved in distilled water, the NH_4^+, H^+ and $W_{12}O_{40}^{8-}$ were introduced in the solution. The pH obtained is approximately 2.5 [3]. The $(H_2W_{12}O_{40}^{6-})$ and $(HW_{12}O_{39}^{5-})$ ions coexist in the solution due to the slight mutual exchange (Table 2) [18]. Generally, it is expected to obtain the optimal mixed effect between in soluble solution of ATM and $ZrOCl_2 \cdot 8H_2O$. However, the AMT are prone to absorb moisture and then cake. It leads to the formation of hard agglomerates with a large particle-size during water evaporation. This occurrence is attributed to the free water molecules drawing the neighboring particles through hydrogen bonds when the particles are sufficiently close. After calcination and reduction, the final ZrO_2 doped W powders would preserve the agglomerate morphology.

Increasing the pH of the original solution to 4 by adding ammonia water under continuous stirring, the $(HW_{12}O_{39}^{5-})$ ions react with the OH^- ions and form pseudo-AMT $(H_3W_6O_{21})^{3-}$. As the pH is further increased to 6, $(HW_6O_{21}^{5-})$ ions are formed through the reaction between $(H_3W_6O_{21})^{3-}$ and OH^-, which easily combines with NH_4^+ to form insoluble APT powder. In previous research [11, 12], M. A. Yar, et al. prepared La_2O_3 and Y_2O_3 doped tungsten powder by adding $Y(NO_3)_3 \cdot 6H_2O$

soluble into ammonium paratungstate (APT). After sintering, their prepared alloys possess greater La_2O_3 particles and the heterogeneous distribution of Y_2O_3 particles. In our previous experiment, the proper amount of ammonia was added into the mixed solution of $ZrOCl_2 \cdot 8H_2O$, $YCl_3 \cdot 6H_2O$ and $(NH_4)_6H_2W_{12}O_{40} \cdot xH_2O$ at room temperature. However, due to the higher reaction rate between Zr^{4+} and Y^{3+} OH^-, the formed composite sol zirconium-yttrium hydroxide $[ZrY(OH)_x]$ result in larger $Zr(Y)O_2$ particle among sintered alloys.

When nitric acid is added to decrease the pH of the AMT solution to below 1, $H_2WO_4 \cdot 2H_2O$ is formed according to the corresponding reactions in Table 2 and then converted into $WO_3 \cdot nH_2O$ by removing water during drying. Due to the slow reaction between $(H_2W_{12}O_{40})^{6-}$ and H^+ at room temperature, thus the hydrothermal method was applied [40-42]. However, after hydrothermal reaction, the reaction product consists of insoluble agglomerate $WO_3 \cdot nH_2O$ microspheres. A novel doping process, which not only can destroy the agglomerate microspheres, but also leads to the uniformed distribution of doping phase, was proposed.
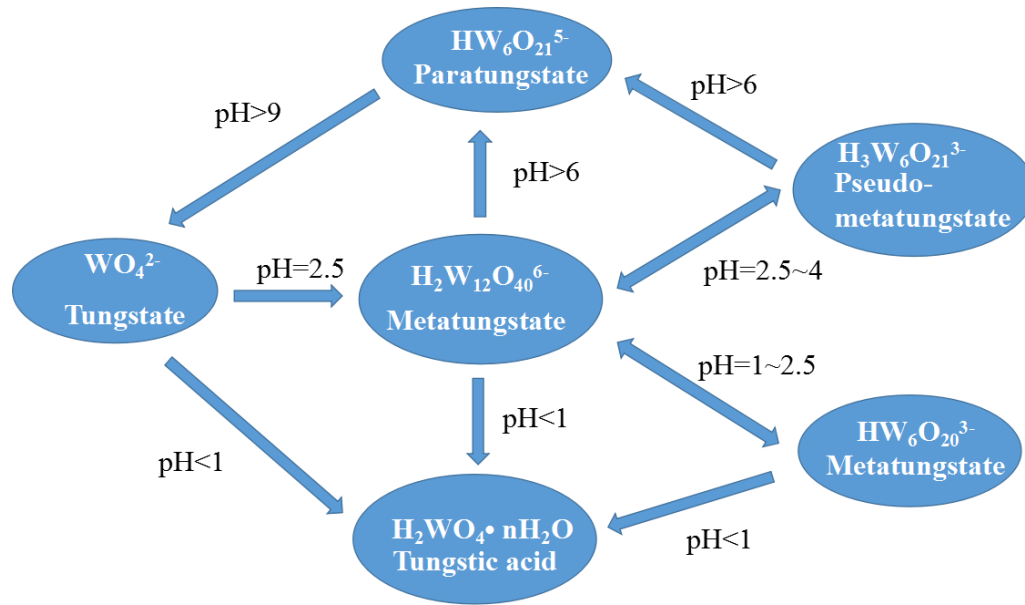
Fig. 1 Schematic diagram of polytungstate species

Table 2 Polytungstate species in solutions containing different pH values.

pH value	Reversible reaction equation	Reaction products	Common name
pH$\leq$1	$(H_2W_{12}O_{40})^{6-}+6H^++32H_2O=12(H_2WO_4\cdot2H_2O)$	$H_2WO_4\cdot2H_2O$	Tungstic acid
pH=2	$H_2W_{12}O_{40}^{6-}+H^+=HW_{12}O_{39}^{5-}+H_2O$	$H_2W_{12}O_{40}^{6-}$ /$HW_{12}O_{39}^{5-}$	Metatungstate
pH=4	$HW_{12}O_{39}^{5-}+2H_2O+OH^-=2(H_3W_6O_{21})^{3-}$	$(H_3W_6O_{21})^{3-}$	Pseudo-AMT
pH>6	$(H_3W_6O_{21})^{3-}+2OH^- = (HW_6O_{21})^{5-}+2H_2O$	$(HW_6O_{21})^{5-}$	Paratungstate
pH>9	$(HW_6O_{21})^{5-}+3H_2O+7OH^-=6(HWO_4)^-+H^++7OH^-=6WO_4^{2-}$ $+7H^++7OH^-$	WO_4^{2-}	Tungstate ion

3.2 Synthesis and analysis of precursor powders

As shown in Fig. 2 a), the undoped precursor powder is composed of radiant microspheres with an average size less than 5 μm. The inset in Fig. 2 a) shows these microspheres are composed of circular or lamellar substances. Containing a small account of (Zr, Y) substances exists of hydrothermal system, the complete

microspheres are destroyed into loose cotton-like powder particles, see Fig. 2 b). XRD patterns of precursor powders, as shown in Fig. 2 c), show that the sharp peaks can be observed, indicating that the synthesized precursor powder exhibits the high-degree crystallinity. All these diffraction peaks can be indexed as hexagonal $(NH_4)_{0.33} \cdot WO_3 \cdot$ (α-HATB, PDF# 42-0452), which agree with the patterns of α-HATB in elsewhere [32]. From the XRD patterns, it can be seen that no any other phases containing Zr and Y elements were detected. Though, $ZrOCl_2 \cdot 8H_2O$ dissolves in strong acid solutions, the hydrolysis of $ZrOCl_2 \cdot 8H_2O$ in aqueous solution still occurs and the Cl^- ions in the outer sphere of the ionic complex are replaced by OH^- groups (Eq. (5))[43].

$$\{[Zr_4(OH)_8 \cdot 16H_2O]^{8+} 8Cl^-\} + 4H_2O = \{[Zr_4(OH)_8 \cdot 16H_2O]^{8+} 8OH^-\} + 8HCl\uparrow \quad (5)$$

Then the $[Zr_4(OH)_8\ 16H_2O]^{8+}$ can react with the hydroxyl ions and form $Zr(OH)_4$ sols [44, 45]. As the $Zr(OH)_4$ sols is amorphous, these aren't detectable in doped precursor [44].

The morphology of the doped precursor was investigated by TEM observation, see Fig. 2 d). A detailed examination reveals that the precursor consists of nanoplate coalescence. The diameter of the synthesized nanoplates is less than 15 nm and their length is less than 100 nm. From the inset in Fig. 2 d), the lattice spacing of hexagonal $(NH_4)_{0.33}WO_3 \cdot H_2O$ is 3.841 Å and identified as the (002) plane. These results indicate the growth of nanoplates along the c-axis direction [45].
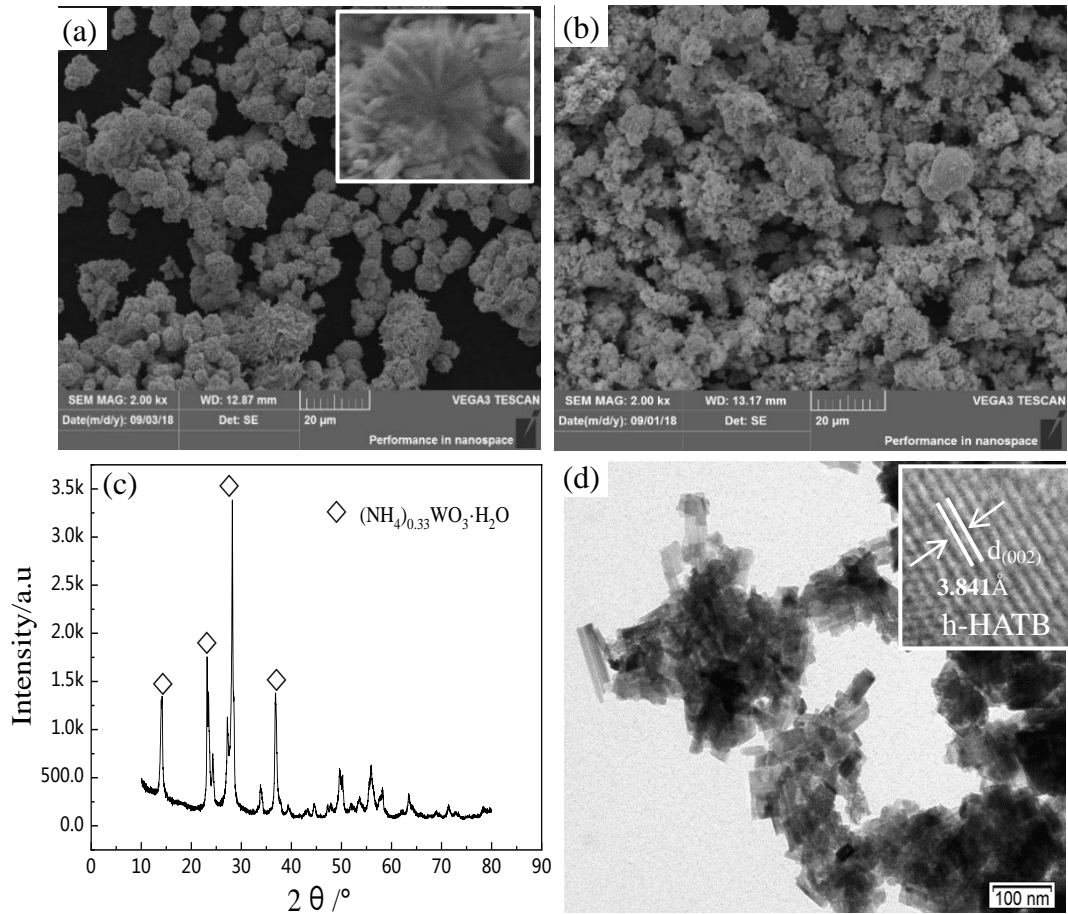
Fig. 2 (a) and (b) SEM images of the undoped and doped precursor powders, (c) XRD patterns of doped precursor powder and (d) TEM image of the $H_{0.75}$ doped precursor.

In this regard, the possible formation mechanism of $(NH_4)_{0.33}WO_3 \cdot H_2O$ nanoplates was proposed. In previous paper of F. N. Xiao and al. [18], the dissolution of $(NH_4)_6H_2W_{12}O_{40} \cdot xH_2O$, in distilled water, introduces $H_2W_{12}O_{40}^{6+}$ and NH_4^+ ions, see next equation Eq. (6).

$$(NH_4)_6H_2W_{12}O_{40} \cdot xH_2O = (H_2W_{12}O_{40})^{6-} + 6NH_4^+ + xH_2O \qquad (6)$$
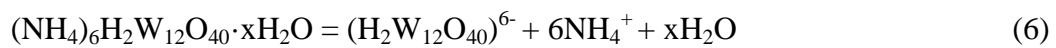
At the beginning of reaction, $WO_3 \cdot nH_2O$ is firstly formed through the hydrothermal reaction of $(H_2W_{12}O_{40})^{6-}$ and H^+ [Eq. (7)].

$$(H_2W_{12}O_{40})^{6-} + 6H^+ + 32H_2O = 12(H_2WO_4 \cdot 2H_2O) \tag{7}$$

The overall reaction was given in the Eq. (8).

$$(NH_4)_6H_2W_{12}O_{40} \cdot xH_2O + 6HNO_3 = 6NH_4NO_3 + 12WO_3 \cdot nH_2O\downarrow + (8-x)\, H_2O \tag{8}$$

$WO_3 \cdot nH_2O$ is formed from the layers of highly distorted corner-sharing $WO_5(H_2O)$ octahedron and interlayer water through hydrogen bonds [40, 41]. The h-WO_3 crystal structure is obtained from hexagonal $WO_5(H_2O)$. Based on the previous research of S. Cao and al. [46], $WO_5(H_2O)$ octahedrons can form three- and six- membered rings by sharing equatorial oxygen in the ab plane (001) (Fig. 3) [42].

In this structure, tungsten atoms are bound to six oxygen atoms in an octahedral coordination. Each oxygen atom is shared by two octahedrons, which are arranged in layers. This finding indicates that numerous hexagonal and trigonal tunnels are distributed in the [001] crystal direction. However, these rings usually stack by sharing the axial oxygen in the c axis [001] and form hexagonal prism (Fig. 3). During nucleation, these primary precipitated crystals from the crystal cell can be generated as a regular hexagonal prism. In the hydrothermal reaction system, the presence of a certain concentration of NH_4^+ ions contributes to occupying the hexagonal tunnels (Fig. 3) [47, 48], and then leads to the accelerated growth of hexagonal-prism WO_3 along the [001] direction and the formation of hierarchical $(NH_4)_{0.33}WO_3 \cdot H_2O$ nanoplates. The nanoplates self-assemble together to form microspheres to reduce the high surface energy [49]. However, it may be due to the addition of doped ions (Zr^{4+}, Y^{3+} and Cl^-) into hydrothermal system, the breakage of order between the positive and negative charge destroys the self-assemble process, leading to the transformation of agglomerated microspheres into relatively dispersed cotton-like precursor.
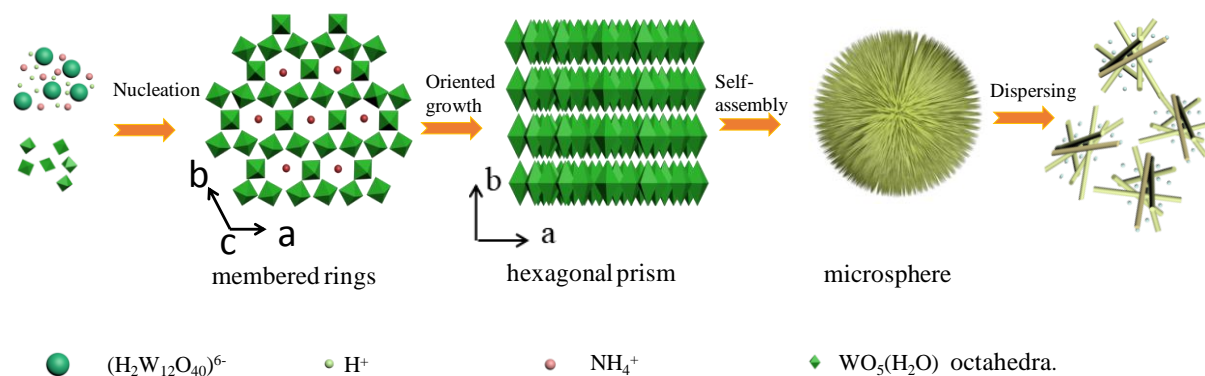
Fig. 3 Schematic diagram of morphology evolution mechanism of $(NH_4)_{0.33}WO_3·H_2O$ precursor.

3.3 Morphology and phase evolution of doped powders during calcination

The TGA and DSC curves of α-HATB were presented in Fig. 4 a). When increasing the temperature to 230 °C, the weight loss may be caused by the loss of surface-adsorbed water at 90 °C and structural water elimination at 175 - 260 °C in the DSC curve (peaks 1 and 2) [52].

From 260 °C to 383°C, a small variation of weight loss was observed. This would be owing to the degassing of NH_3 molecules due to the partial $(NH_4)_{0.33}WO_3·H_2O$ decomposition. However, it was reported that α-HATB powder can be produced after calcining APT at 400 °C under hydrogen atmosphere [53], so the degassing of NH_3 below 400 °C was unexpected. Up to 430 °C, an obvious weight loss occurs quickly. This may be due to the partial NH_3 molecular rearrangement occurred in a solid state chemical equilibrium reaction, causing partial NH_3 molecules to transfer to the surface of α-HATB particles and then leading to the complete decomposition of $(NH_4)_{0.33}WO_3·H_2O·H_2O$. However, it's not like that the flat horizontal TGA line at above 430°C, it can also be seen that the exothermic peak 3 could be observed at 500°C in DSC results. This indicated a phase transition, see Fig. 4 a) [52]. Due to most of the NH_3 getting rid of hexagonal channel, it leads to the collapse of hexagonal structure and the transform from α-HATB into monoclinic WO_3 (m-WO_3) [54].

In order to confirm the speculation above-mentionned, the phase evolution of the $H_{0.5}$ powders calcined at 400 ~ 500 °C, in inert Ar atmosphere, was studied. The calcined powders were hereafter abbreviated as CP samples in Fig. 4 b). When heated to 400°C, although the NH_3 and H_2O release, the α-HATB structure does not change, indicating that there are still some NH_3 molecules in the hexagonal channels. When heated to 430°C, the peak intensity of α-HATB at about 15° decreases. Meanwhile, the m-WO_3 occurs. When calcined at 470 °C, the peak intensities of α-HATB continue to decline. Up to 500°C, the α-HATB has almost completely disappeared and the powder mainly consists of m-WO_3. It's worth noting that during phase evolution, α-HATB directly transforms into monoclinic m-WO_3 without the formation of intermediate phase h-WO_3. It indicates that NH_4^+ or NH_3 in the hexagonal channels are indispensable for stabilizing the hexagonal structure. During calcining, the hexagonal channels become gradually empty, leading to the collapse of the hexagonal framework and the formation of m-WO_3 [32, 54].
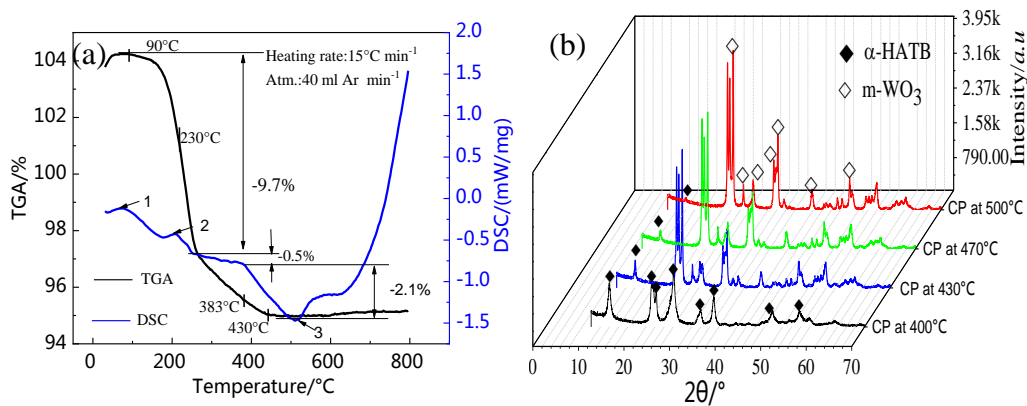
Fig. 4 (a) The TGA and DSC curves of the decomposition of the $H_{0.5}$ precursor powder and (b) XRD patterns of doped powder after calcination at different temperature for 2 h.

3.4 Phase and morphology evolution of reduced powders

The XRD patterns of the reduced $H_{0.5}$ powders obtained directly from doped precursor by the hydrogen reduction at 500 ~ 950 °C are shown in Fig. 5. The reduced powders were hereafter abbreviated as RP samples in Fig. 5. Some characteristic

parameters of the $H_{0.5}$ powder prepared through different reduction processes were listed in Table 3. From the XRD patterns of the powder reduced at 500 °C, it can be seen that the powder mainly consists of hexagonal $(NH_4)_{0.42}WO_3$ (β-HATB) phase. No m-WO_3 peaks can be indexed. All the diffraction peaks of β-HATB agree well with the standard data file (PDF#42-0451, a=0.7359 nm, b=0.7359 nm, c=0.7544 nm), which is also in consistent with the patterns of β-HATB in elsewhere [32]. Generally speaking, under high temperature (i.e. above 430°C), the hexagonal structure collapses due to the release of the NH_3. However, in reductive atmosphere, these anoxic environments hinder the formation of m-WO_3 and promote the occurrence of the β-HATB. However, the structure of β-HATB was disputed [32]. As so far, there are two different PDF# cards assigned to it. They are $(NH_4)_{0.06}WO_3 \cdot (H_2O)_{0.11}$ (PDF#15-0217) and $(NH_4)_{0.42}WO_3 \cdot H_2O$ (PDF# 42-0451), respectively. When the temperature increases to 550 °C, the weaker intensities of $W_{20}O_{58}$ peaks indicate that a tiny amount of β-HATB powder transform into $W_{20}O_{58}$ powder. When heated to 650 °C, the patterns of powder significantly have changed compared to the previous two powders. β-HATB and $W_{20}O_{58}$ phases are disappeared. The powder mainly consists of $WO_{2.0}$ and W phase. Three peaks of W phase can be observed at 40.26° (110), 58.27° (200) and 73.19° (211) corresponding to the α-W phase (PDF#04-0806). This finding indicates that the nucleation and growth of $WO_{2.0}$ and α-W phases from the precursor occur at reduction temperature of 550 - 650 °C. Moreover, detailed examination shows that there are three weak diffraction peaks at 35.59° (004), at 43.97° (211) and 69.7° (321), respectively. All these peaks correspond to β-W phase (PDF#47-1319). Hu et al. [15] reported that the β-W phase transformed into α-W at 520 - 625 °C. It indicates that in this current research, the transformation temperature of β-W into α-W increases, which may be due to the addition of containing (Zr, Y) phase.

When heating the doped powder to 750 °C, the WO_2 peaks become weaker, whereas peaks of the α-W become stronger. Up to 800 °C, the WO_2 completely disappears and the powder consists of the α-W phase as shown Fig. 5 b). However, the peak intensities of the α-W phase are still weaker compared to powders reduced at

850 °C and 900 °C, respectively. With heated to 900 °C, the peak intensities of the α-W powder remain almost unchanged compared with those of the powder reduced at 950 °C, indicating that the doped powder reduced at 900 °C has complete crystallinity. As a result of the above analysis as listed in Table 3, α-HATB is reduced to W in the range of 500 - 900 °C through the reduction sequence of α-HATB→β-HATB→$W_{29}O_{58}$→WO_2→(β-W) α-W. It's worth noting that among these phase transitions, the phase transitions of HATB→$WO_{2.9}$ and $WO_{2.9}$→WO_2, is very fast and the overall transition rate of HATB→W is limited by $WO_2 \rightarrow W$ [30].
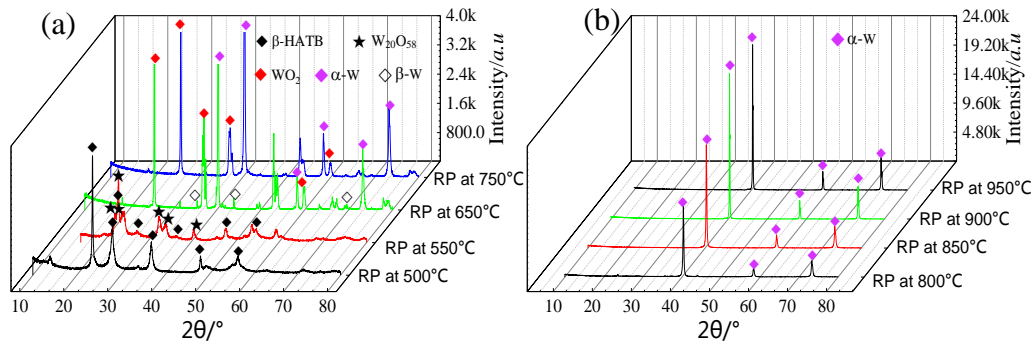
Fig. 5 (a) XRD patterns of tungsten powders reduced at 550-750 °C for 1.5 h and (b) XRD patterns of tungsten powder reduced at 800 - 950 °C for 2 h.

Table 3 Characteristic parameters of $H_{0.5}$ powder prepared through different reduction processes at varying temperature from 550 to 900°C.

Reduction tempe.	500 °C	650 °C	750 °C	800 °C	850 °C	900 °C
Composition	β-HATB	α-W, β-W, WO_2	α-W WO_2	α-W	α-W	α-W
[d_{50}] /μm	-	-	0.125	0.926	1.12	1.57
Crystallite size (Å)	218(3)	316(3)	503(3)	662(21)	565(7)	1164(42)
SSA ($m^2 \cdot g^{-1}$)	-	-	3.265	2.765	2.673	0.213

The morphologies of the doped powders obtained by different reduction processes at varying temperature from 550 to 800 °C are shown in Fig. 6 a), b), c) and

d). The doped powder reduced at 550 °C has the similar morphology with that of calcined powder, which also preserves the morphology of precursor powder. Increasing the temperature to 650 °C, a little change in the morphology is observed, see Fig. 6 b). However, combined on the XRD result, close examination reveals that the powder is composed of agglomerates, consisting of nanosized tungsten or tungsten oxide crystals. Observations in the micro-morphology don't reveal differences in their actual crystalline structure. With increasing temperature up to 750 °C, the doped powder consists of nanosized particles as shown in Fig. 6 c). The nanosized particles are distinguishable as marked by the white square. This is enhanced due to the chemical vapor transport (CVT), causing the formation of distinct, nanosized and single crystals [28]. Increasing the temperature to 800 °C provokes that the α-W powder exhibits two different particle morphologies due to grain growth: the ratio of rod length to mill diameter is about 5 and equiaxed flaky particles with a mean particle size of the order of 0.93 μm as shown in Fig. 6 d) and Table 3. Seen from figures 6 c) and d), the morphologies of two kinds of powder greatly change due to that reduction temperature has significant effects on the size and composition of the doped tungsten oxide powders. During the reduction process, H_2 molecules enter into the inner of loose precursor powder, reacting with α-HATB and then forming intermediate phases of tungsten oxide, elementary W and H_2O vapor. The reduction from α-HATB to W goes through five reaction steps (see relationship 9 - 13), i.e., α-HATB→β-HATB, β-HATB→$W_{29}O_{58}$, $W_{29}O_{58}$→WO_2, WO_2→$WO_2(OH)_2$ and $WO_2(OH)_2$→W.
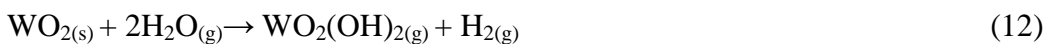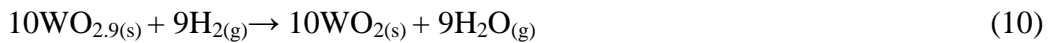
$$10WO_{3(s)} + H_{2(g)} \rightarrow 10WO_{2.9(s)} + H_2O_{(g)} \qquad (9)$$

$$10WO_{2.9(s)} + 9H_{2(g)} \rightarrow 10WO_{2(s)} + 9H_2O_{(g)} \qquad (10)$$

$$WO_{2(s)} + 2H_{2(g)} \rightarrow W_{(s)} + 2H_2O_{(g)} \qquad (11)$$

$$WO_{2(s)} + 2H_2O_{(g)} \rightarrow WO_2(OH)_{2(g)} + H_{2(g)} \qquad (12)$$

$$WO_2(OH)_{2\ (g)}+3H_{2(g)} \rightarrow W_{(s)}+ 4H_2O_{(g)} \tag{13}$$

In the first three intermediate phase transformations at low reduction temperatures, the powder composition and tungsten atomic position have almost not changed, leading to the slightly difference in powder morphologies. Due to continuous increase the temperature, H_2O vapor reacts with WO_2 to form volatile $WO_2(OH)_2$ [Eq. (12)], leading to the occurrence of CVT process. Through short-range CVT, the tungsten atoms from WO_2 deposit on the neighbor oxide particles. The growth rate of tungsten powder particles depends on the concentration of $WO_2(OH)_2$ and CVT rate, which are affected by the hydrogen gas flow rate and reduction temperature, respectively [5,55].
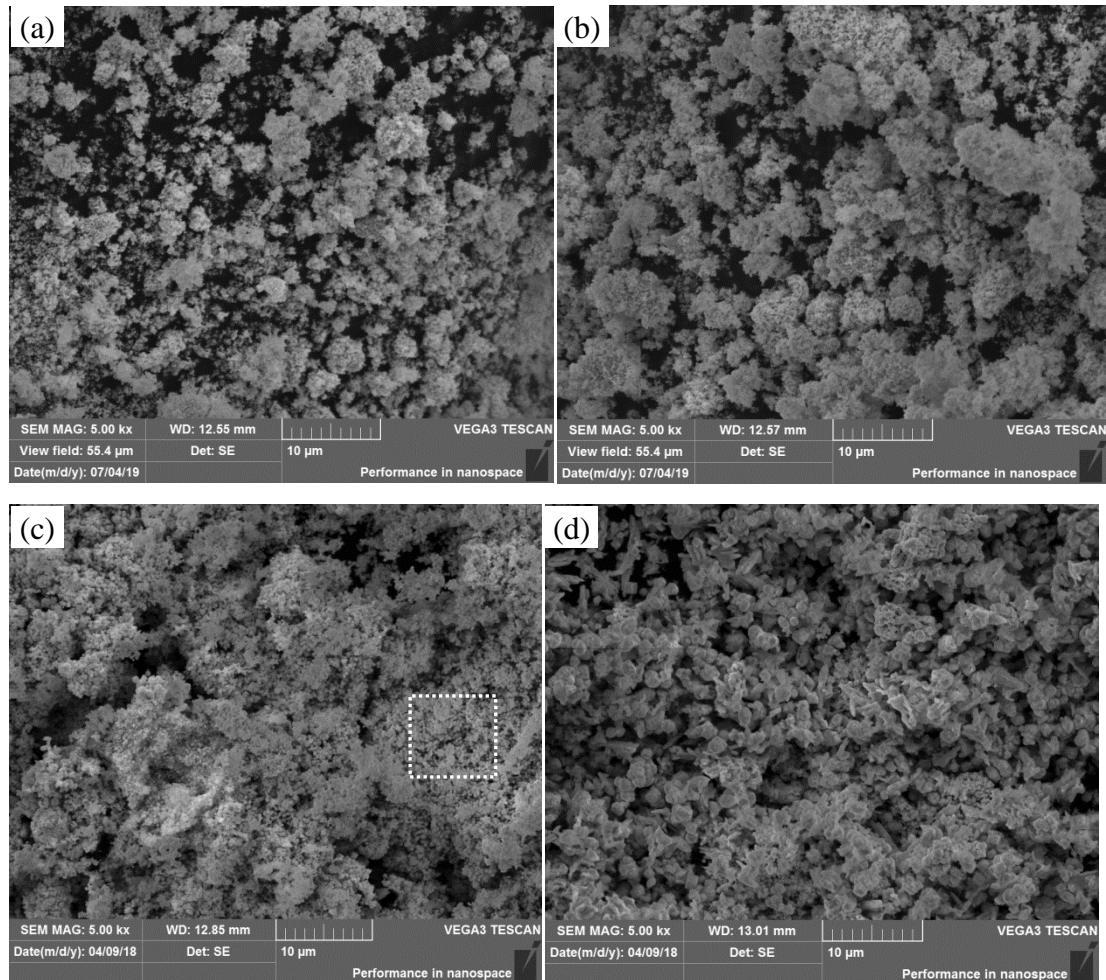
Fig. 6 Change of particle morphologies of doped powders obtained by different reduction processes at varying temperature: (a) 550 °C, (b) 650 °C, (c) 750 °C and (d) 800 °C, respectively.

3.5. Analysis of phase and morphology of the W-Zr(Y)O$_2$ powders

XRD patterns of doped tungsten powders prepared through the reduction process of 500 °C (1.5h) + 900 °C (2h) have been compared plotted in Fig. 7. The characteristic parameters of these powders were summarized in Table 4, such as crystallite size, specific surface area, full width at half maximum and the parameters of PSD.

As the tiny amount of Zr(Y)O$_2$ (the doping amount is less than 0.75%) was doped in powders, no diffraction peaks of containing (Zr, Y) phases can be found. Thus, 5% wt Zr(Y)O$_2$ was designed to determine the composition of doped tungsten powder. The XRD patterns of H$_{5.0}$ powder indicate that the doped tungsten powders consist of α-W and cubic ZrO$_2$ (c-ZrO$_2$). With the increase in Zr(Y)O$_2$ content to 0.5 wt%, the tungsten particles are refined gradually through SEM observation as shown in Fig. 8. The refinement effect can also be confirmed by the reduced crystallite size and d$_{BET}$ as listed in Table 4. The comparison of the FWHM of five powders reveals a slight increase in peak broadening with increasing in Zr(Y)O$_2$ content as shown in Fig. 7 and Table 4, which were mainly caused by the fine particle size [3, 56].
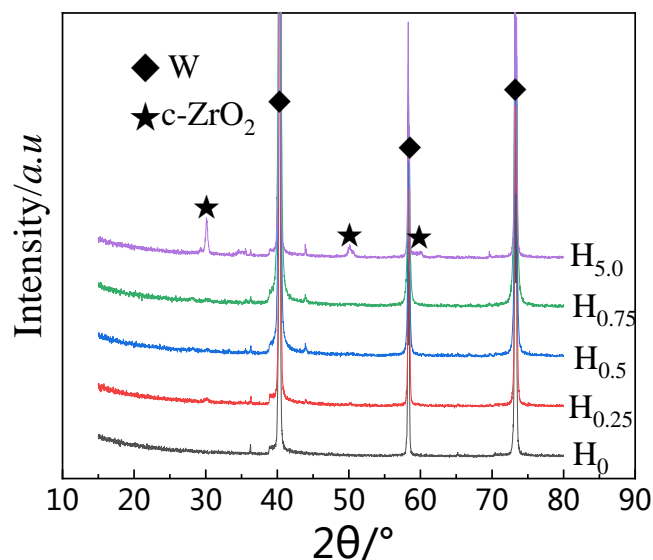
Fig. 7 XRD patterns of five doped powders after reduction at 900 °C for 2 h.

The undoped W powder particles having a polyhedral shape, see Fig. 8a). The surface of particle is smooth. However, the surface of the nearly spherical doped W

powder particles is rough compared with that of undoped W particles. Moreover, compared to the undoped powder, the distinguishable quantitative comparison of particle profile indicates a low degree of agglomeration. Detailed examination shows that the surfaces of the doped powder particles exhibit some white nanosized substances, see inset in the Fig. 8 d) (arrow A in inset).

The EDS results reveals that the atomic ratio of Zr(Y) to O was in a ½ molar ratio, as shown in Fig. 8 e). It indicates that these nanosized substances are mainly $Zr(Y)O_2$. From Fig. 8 f), it can be also seen that as $Zr(Y)O_2$ content increases, the crystalline size and the mean particle size [d_{50}] both decrease firstly and then increase slightly. However, the crystalline size of the four powders is about 15-20 times less than the mean particles size, see Table 4).

Table 4 Characteristic parameters of the four doped powders reduced at 900 °C for 2h.

Samp.	Crystallite sizes(Å)	FWHM	SSA $(m^2 \cdot g^{-1})$	d_{BET} (μm)	d_{10}/ μm	d_{25}/ μm	d_{50}/ μm	d_{75}/ μm	d_{90}/ μm	F_{ag}
H_0	1404	0.134	0.235	1.32	1.37	1.09	2.76	4.53	6.52	2.09
$H_{0.25}$	1164	0.174	0.289	1.12	0.95	0.85	1.91	2.60	4.15	1.71
$H_{0.50}$	1065	0.176	0.213	1.46	0.81	1.05	1.57	2.52	3.32	1.08
$H_{0.75}$	1099	0.189	0.372	0.83	0.79	1.23	1.73	2.62	3.95	2.08

To analyze the distribution of W and the doping phase $Zr(Y)O_2$, EDS mapping was conducted on W-0.75% $Zr(Y)O_2$ powder as shown in Fig. 9. The W and Zr elements have more obvious signal strength compared to Y element with law Y content in powder, see Fig. 9 d). This would be owing to the tiny Y content in powder. Moreover, Zr and Y coexist in same W particles, suggesting $Zr(Y)O_2$ is uniformly distributed in doped powder, see Fig. 9(b-d).
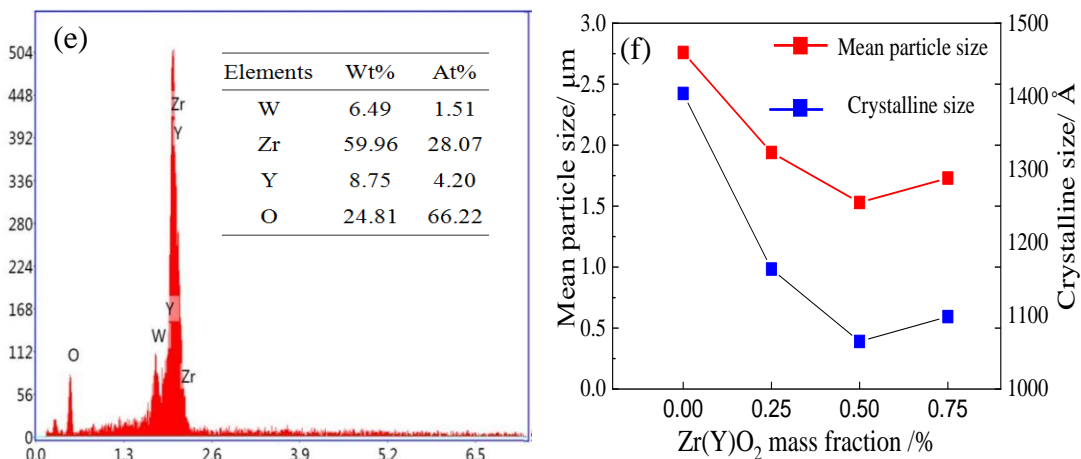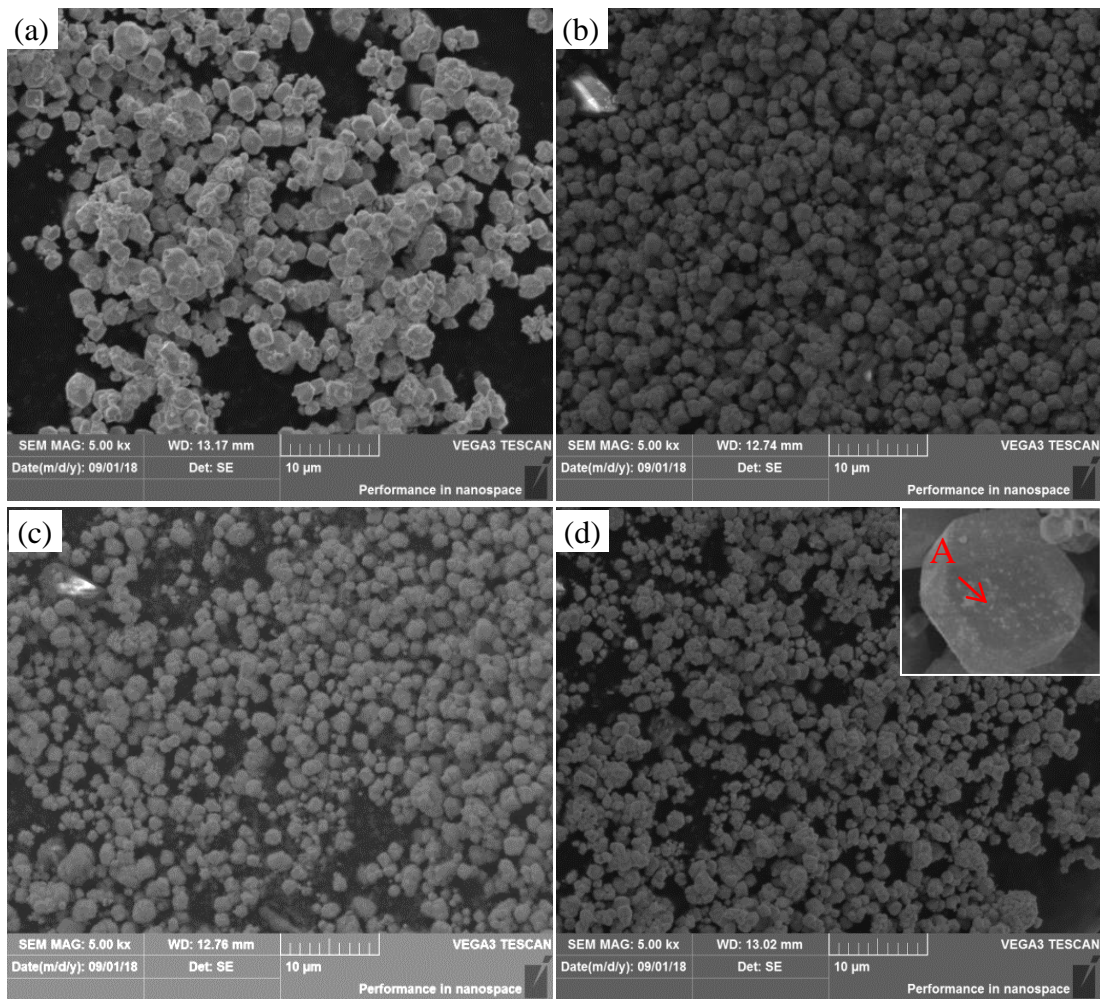
Fig. 8 Morphologies of doped tungsten powders: (a) Pure W, (b) W-0.25 wt% Zr(Y)O$_2$, (c) W-0.5 wt% Zr(Y)O$_2$, (d) W-0.75wt% Zr(Y)O$_2$, (e) EDS pattern of the nanosized substance of red arrow A and (f) Mean particle size and crystalline size vs. Zr(Y)O$_2$ contents.
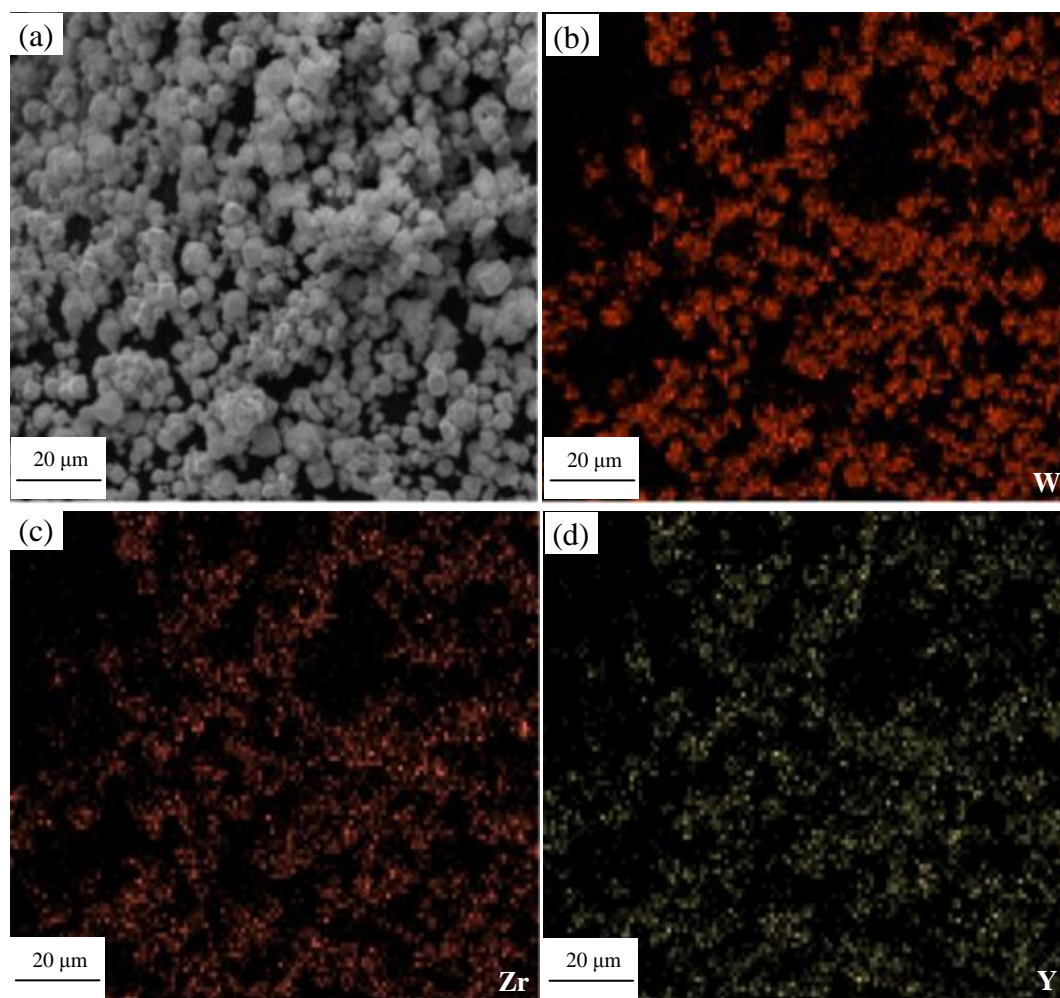
Fig. 9 Elemental distributions of the W-0.75wt% Zr(Y)O$_2$ powder.

Crystalline structural details were revealed by TEM and HR-TEM observations conducted on the H$_{0.5}$ powder sample. The observation of the nanosized particles shows nearly-spherical morphology in Fig. 10 a). The statistical distribution of the particle size histogram is based on 300 particles from different TEM images, see Fig. 10 b). The diameters of more than 90% of particles range from 6 nm to 50 nm with the average particle size of 28 nm.

The crystal planes correspond to the (110) planes of α-W shown by the HR-TEM image in Fig. 10 c). The measured lattice spacing is about 2.313 Å. As shown in Fig. 10 d), the value of the measured lattice spacing of 3.030 Å agrees well with the (111) lattice spacing of cubic ZrO$_2$ [d(111)=2.965 Å, PDF#49-1642]. Previous research revealed that the synthesized cubic ZrO$_2$ may result from the doping process.

Clustering ZrO_2 and Y_2O_3 is the premise of forming stabilised ZrO_2 phase [58]. So it is easy to understand that the doping process described in the experimental section for synthesis of the precursor powders was used to obtain containing Zr and Y phase close together.
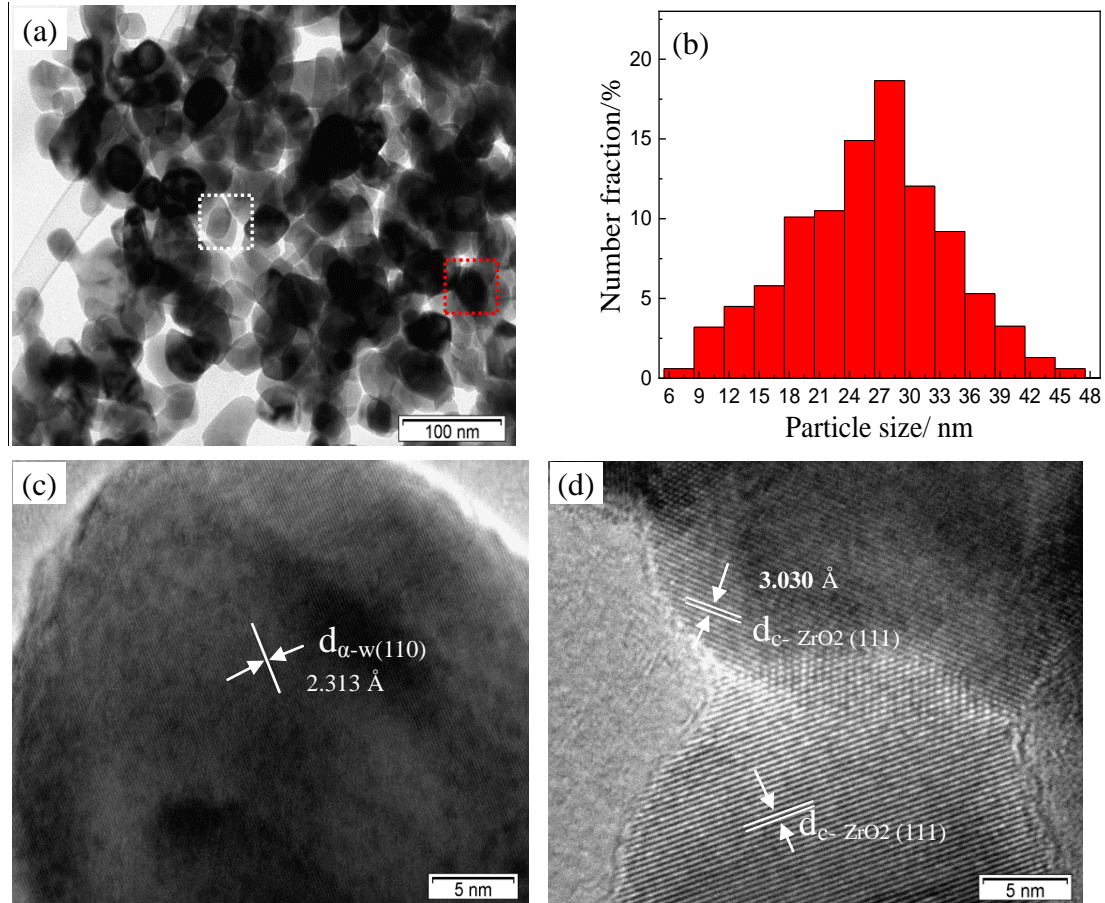
Fig. 10 (a) TEM images of the W-0. 5% Zr(Y)O_2 powder, (b) Size distribution of nanosized particles, (c) and (d) HR-TEM images conducted on selected area marked by red and white squares in Fig. 10 a), respectively.

Frequency distribution curves of doped powders are illustrated in Fig. 11 a), b), c) and d). All showing a state of normal distribution and the curve is unimodal (i.e., single peak curve). Most pure tungsten powder particles with a particle size ranging from 1.09 to 4.53 μm with d_{50} of 2.76 μm were obtained. For the W-0.5% Zr(Y)O_2 powder, 75% of tungsten powder particles were reached to 3.52 μm in size and its d_{50} is about 1.57 μm, see from Fig. 11 a). The reduced particle size is due to the

refinement effect of $Zr(Y)O_2$. However, when the $Zr(Y)O_2$ content increases up to 0.75%, its d_{50} and d_{75} were achieved to 1.73 μm and 2.62 μm, respectively.
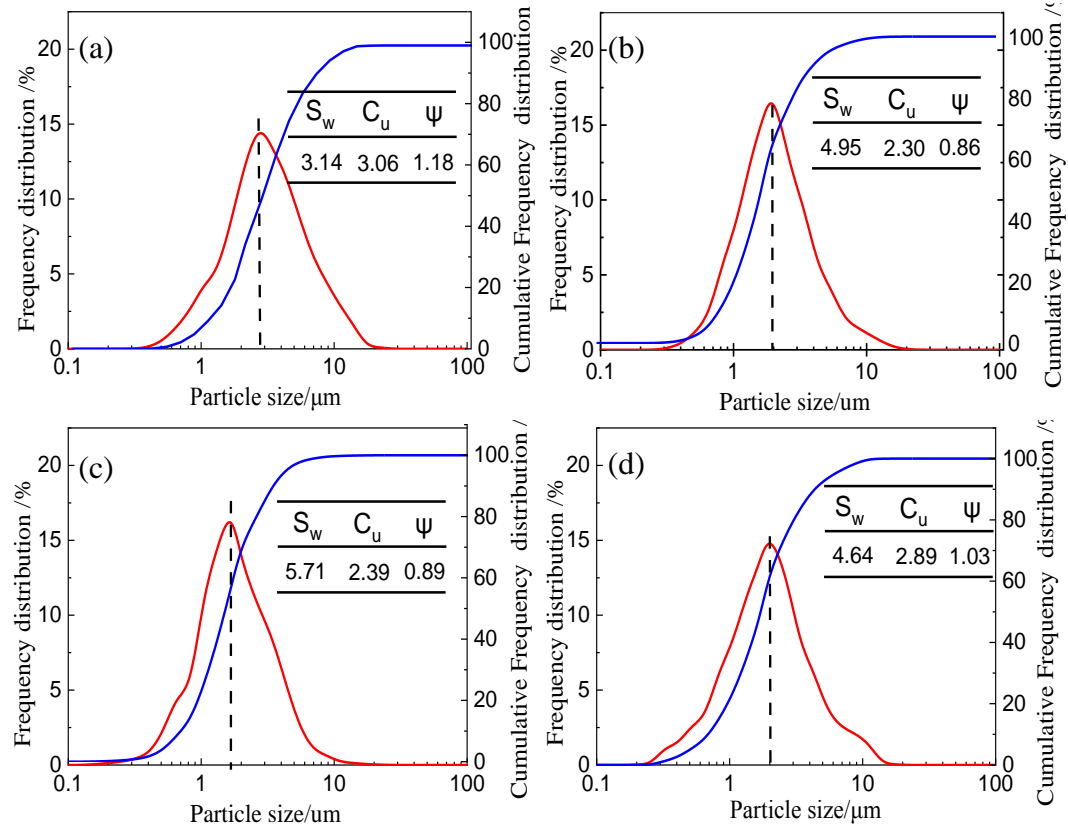
Fig. 11 PSDs of W-$Zr(Y)O_2$ powders with different $Zr(Y)O_2$ contents: (a) 0, (b) 0.25% $Zr(Y)O_2$, (c) 0.5% $Zr(Y)O_2$ and (d) 0.75% $Zr(Y)O_2$.

In order to observe the PSD characterization more intuitively, PSD parameters of four doped powders were illustrated in Fig. 12 a) and b). The 75% of the doped powder particles are smaller than 3 μm in size with their d_{50} less than 2 μm. It indicates that the narrower size distribution and the smaller average particle size among doped powders. The histogram of distribution slope parameter (S_w), coefficient of uniformity (C_u) and span value ($Ψ$) of four powders is shown in Fig. 12 b). The determined S_w values of the H_0, $H_{0.25}$, $H_{0.5}$, $H_{0.75}$ powders were 3.14 μm, 4.95 μm, 5.71 μm and 4.64 μm, respectively, indicating that the S_w values of doped powders is larger than that of pure powder. However, it is reported that the larger the S_w value, the narrower the PSD. Generally, powders with S_w value of 2 indicate a very broad

distribution and the powders with S_w value between 4 and 5, are usual process conditions used as raw materials for manufacturing non-defective injected components by Powder Injection Moulding Process [9, 57, 58]. On the contrary, the lower the C_u value, the narrower the particle sizes-distribution [10]. Thus, the value of C_u reduces from 3.06 to 2.30, indicating the narrower PSD. It can be also confirmed by the reduced value of Ψ from 1.18 to 0.86 [39]. It's worth noting that the reduced values of C_u and Ψ show a non linear variation, this is due to that the different $Zr(Y)O_2$ doping amount results in the different refinement effect. Excessive $Zr(Y)O_2$ would cause the agglomerates' formation of refined particles [59]. However, as listed in Table 4, the agglomeration factors (F_{ag}) of the doped powders, indicating the agglomerate state, are less than 3, which means the particles were little agglomerated [60].
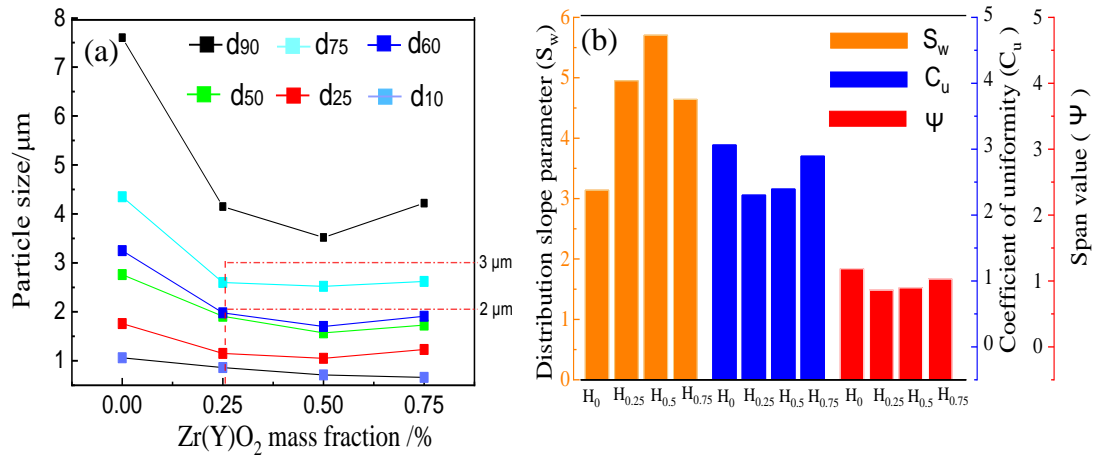
Fig. 12 PSD parameters of four W-$Zr(Y)O_2$ powders: (a) Particle sizes at the different cumulative volume percentage vs. $Zr(Y)O_2$ content and (b) Distribution slope parameter, coefficient of uniformity and span value vs. $Zr(Y)O_2$ contents.

3.6 Microstructure of alloys

The effect of sintering temperature on microstructure of the W-0.25 wt. % $Zr(Y)O_2$ alloy produced by spark plasma sintering process with various final temperatures from innovative developed powder was investigated. As through fracture surfaces, oxide particle cannot be obviously observed, the SEM images of the etched microstructure, are presented as shown in Fig. 13(a-d). Fig. 13 a) shows the plenty of necks and interconnected pores in the samples. After sintering at 1900 °C, the grain size slightly increases from 1.5 μm to 2.2 μm, which may result from the accelerated diffusion process due to the combined effects of higher pressure and high temperature. However, after sintering at 2000 °C, the grains size and relative density increased rapidly. It indicates the rapid densification of the tungsten powder in the temperature range of 1900~2000 °C under 30 MPa, in which the change trend of grain size and density matched well with the case of micro-hardness inflection-point. The average grain size of alloy sintering at 2000 °C is 4.7 μm, smaller than that of pure tungsten (8.5 μm) [61]) under the same sintering process, suggesting that oxide particles cause the refinement effect on grain growth of high temperature sintering process. Further increasing temperature to 2100 °C, the grain size and density continuously increase and the average grain size reaches the value of 6.3 μm.

The curves of grain size and relative density obtained by SPS with various final temperature were plotted in Fig. 14 a). It is worth noting that in the etched microstructure, a lot of white particles were observed. These white particles are $Zr(Y)O_2$ particles confirmed by the EDS analysis using the same methodology and the same case study as F. N. Xiao et al. [18]. The PSD of $Zr(Y)O_2$ of the corresponding alloy manufactured by via SPS sintering, at 2000 °C for 5 minutes in Fig. 14 b). These results confirm that more than 95% of particles are less than 500 nm with an average particle size of 250 nm. Among these $Zr(Y)O_2$ particles, some larger oxide particles are located at or near the grain boundaries (marked by white arrows in Fig. 13 c), which induced stress/strain concentrations as the starting points of possible cracks and reduce the fracture toughness of material [62]. However, as shown from the inset in

Fig. 13 c), lots of nanosized oxide particles as marked by red arrows are homogeneously distributed within the grains. In fact, in standard TEM observation as shown in Fig. 14 c) (indicated by solid arrows), a large number of particles were found in grains. HR-TEM images based selected area electron diffraction pattern (SAEDP) from selected area under the red box in Fig. 14 c) reveal the white particles were obtained in the presence of cubic phase of nanocrystalline ZrO_2, which may be caused by the diffusion of Y element into containing Zr phase during high-sintering temperature. These particles can generate, hinder and then accumulate dislocations during the deformation process. The particles exhibit a good bonding with the tungsten phase. However, there are no coherent relationship between tungsten phase and oxide phase, see Fig. 14 d).
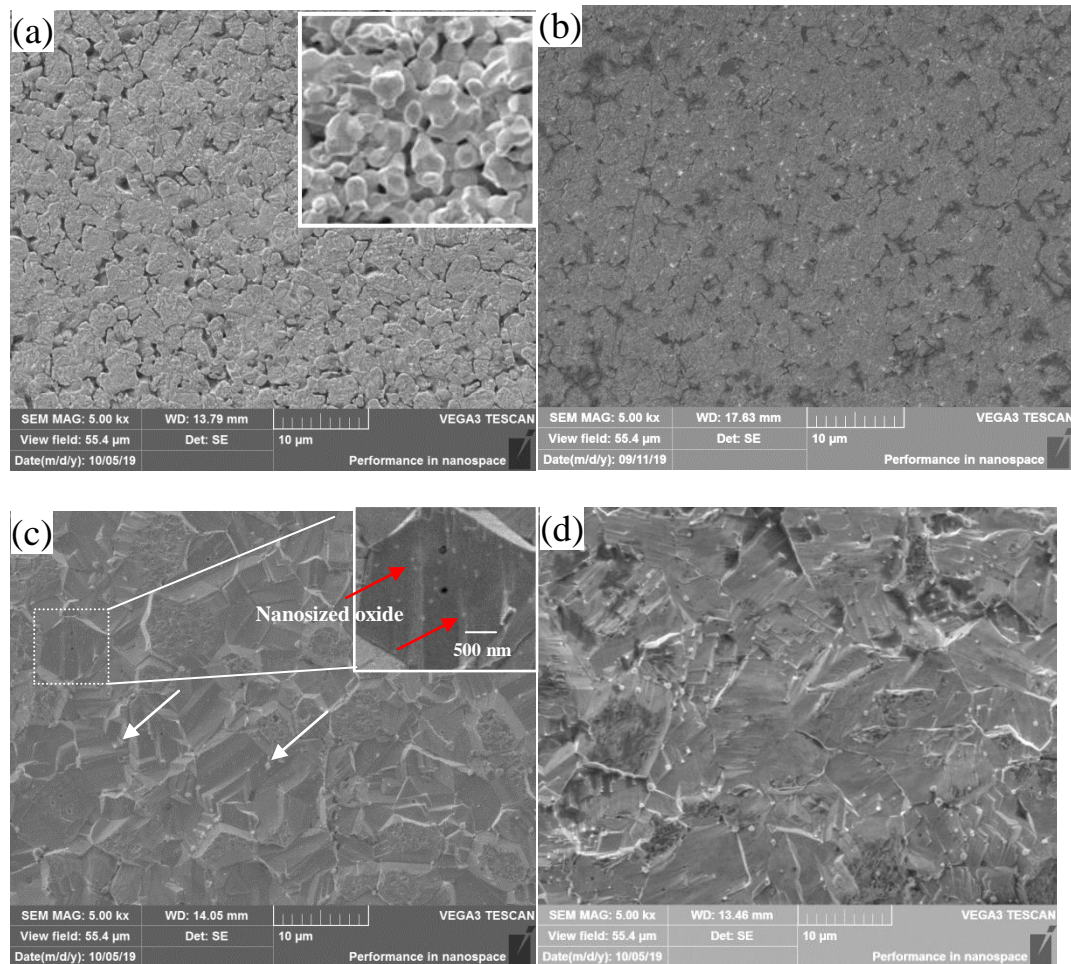
Fig. 13. Microstructure of alloys produced by different spark plasma sintering processes with various final temperatures: (a) 1800 °C for 5 min, (b) 1900 °C for 5 min, (c) 2000 °C for 5 min and (d) 2100 °C for 5 min.
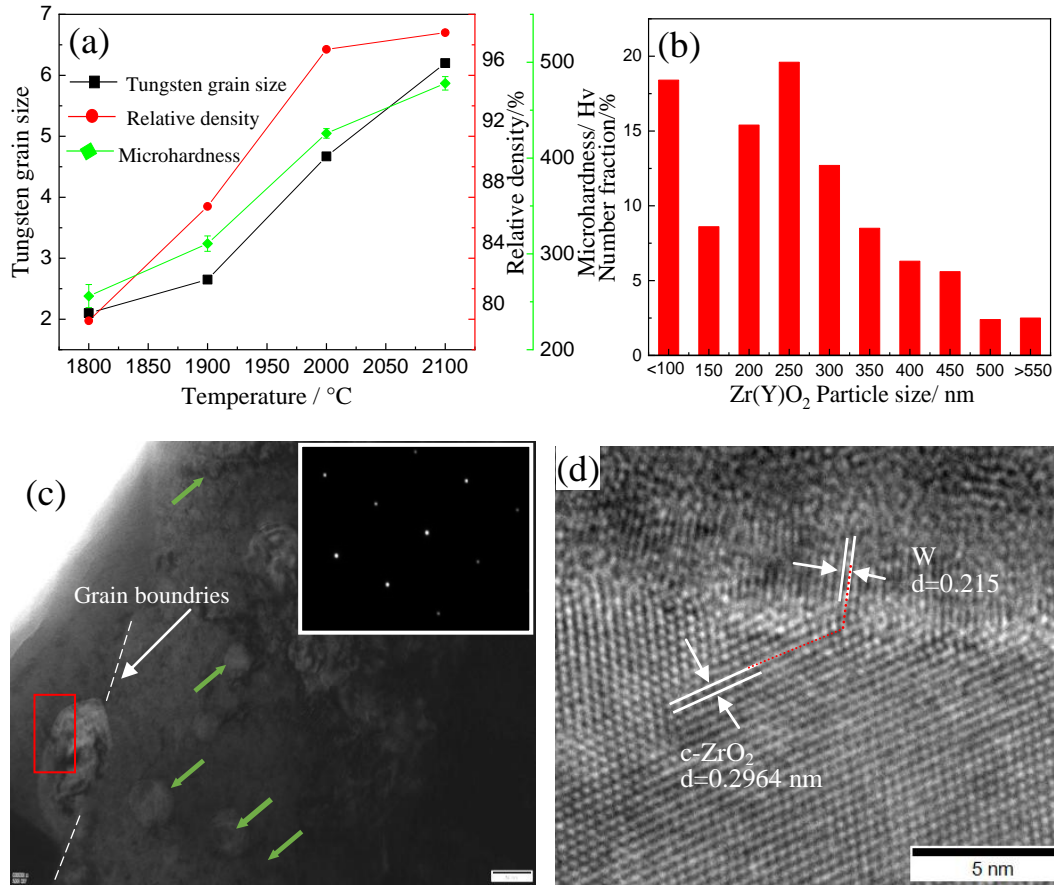
Fig. 14 (a) Evolution of tungsten grain, relative density and microhardness of alloy vs alloys sintered under different conditions, (b) PSD of $Zr(Y)O_2$ in alloy, (c) TEM images of tungsten alloy conducted of sintered alloy at 2000 °C and (d) HR-TEM image of $Zr(Y)O_2$/W interface.

Ultrafine and nanosized $Zr(Y)O_2$ particles dispersed in current tungsten alloy may be due to the high quality doped powder prepared by composite hydrothermal method. The powder particles surfaces are covered each of the white substances, see Fig. 8 d). Sintered under 1800 °C, these white substances have the similar size as the oxide particles as shown Fig. 13 b). With increasing sintering temperature to 1900 °C, the nanosized white substances agglomerate slowly. The same case can be found in references [37, 61, 63]. Moreover, the content of oxide particle also affects the eventual oxide particle size. In references [63, 64], the effect of oxide particle content on microstructure of the ODS-W alloy through different processes was investigated. Therefore, it can be confirmed that larger particles are formed by the aggregation of small particles at high temperature sintering.

The initial oxide particle size in doped tungsten powders, mainly deponds upon the doping techniques. SPS, HIP and sintering in vertical direction (VD) processes regarded as a rapid sintering process, can reveal the initial oxide particle size in doped tungsten powders to some extent. Wang et al. [37, 61] prepared the W-ZrO$_2$ and W-Al$_2$O$_3$ alloys through separately hydrothermal method combined with SPS sintering process. Due to the serious agglomeration of precursor powder, Al$_2$O$_3$ and ZrO$_2$ can not be evenly distributed in powders. It leads that coarse and adhesive oxide particles (areas marked by a red circle) and reaches to value of 3 μm in alloy as shown in Fig. 15 a) and b). It indicates that using separately hydrothermal method cannot obtain the ultrafine and uniformly distributed oxide particle in powders compared to the proposed methods in this current research. In this case study, W-ZrO$_2$ powder were manufactured by azeotropic distillation method, followed by the vertical direction, the ZrO$_2$ particles still reach the value of 1.0 μm, which may result from agglomerated W-ZrO$_2$ powders [37, 65].

A novel fabricated method was developed to elaborate W-Zr(Y)O$_2$ alloy and was compared of the tradionnal methods to produce some oxide dispersion-strengthened tungsten alloys manufacturing by fast sintering processes, as listed in Table 5. These alloys listed in Table 5 were prepared via other liquid-liquid, liquid-solid or solid-solid (mechanical alloying) doping methods, respectively.

Seen from Table 5, using liquid-liquid doping processes, can achieve smaller oxide particle compared to conventional mechanical alloying. However, the average particle size of alloys through the liquid-liquid methods, which are different from the proposed method, still reach up to 1.5 μm, 3.5 μm and 3.6 μm, respectively. For mechanical alloying of ODS-W powders, the refinement effect on oxide particle size is limited to some extent even through doping nanosized oxide particles [68,70]. Angel Muñoz et al. [68] prepared the W-La$_2$O$_3$ powder using nanosized La$_2$O$_3$ particles ranging from 10 to 50 nm in size as raw material. However, the large adsorption effect of nanosized oxide particles leads to the formation of particle aggregations even after ball-milling for 30 hours [70]. For the liquid-solid doping processes, they are usually expected to obtain smaller oxide particles size. However,

in the W-La$_2$O$_3$ alloys prepared through SPS process and sintering in the vertical direction, respectively [11, 66], both La$_2$O$_3$ particles exceeding 2 μm. Yar M.A. et al. prepared the nanosized Y$_2$O$_3$ particle reinforced tungsten alloy through liquid-solid doping processes [12], oxide particles were non-uniformly distributed into the tungsten matrix due to the reaction occurred only at the surfaces of APT as shown in Fig. 15 d). In current research, the oxide particles in tungsten alloy are 0.8-10 times smaller than those in published alloys. Moreover, a large number of the nanosized oxide particles are observed within tungsten grains, see inset in fig. 13c), indicating the proposed novel liquid-liquid doping process is the appropriate to reduce the particles size.
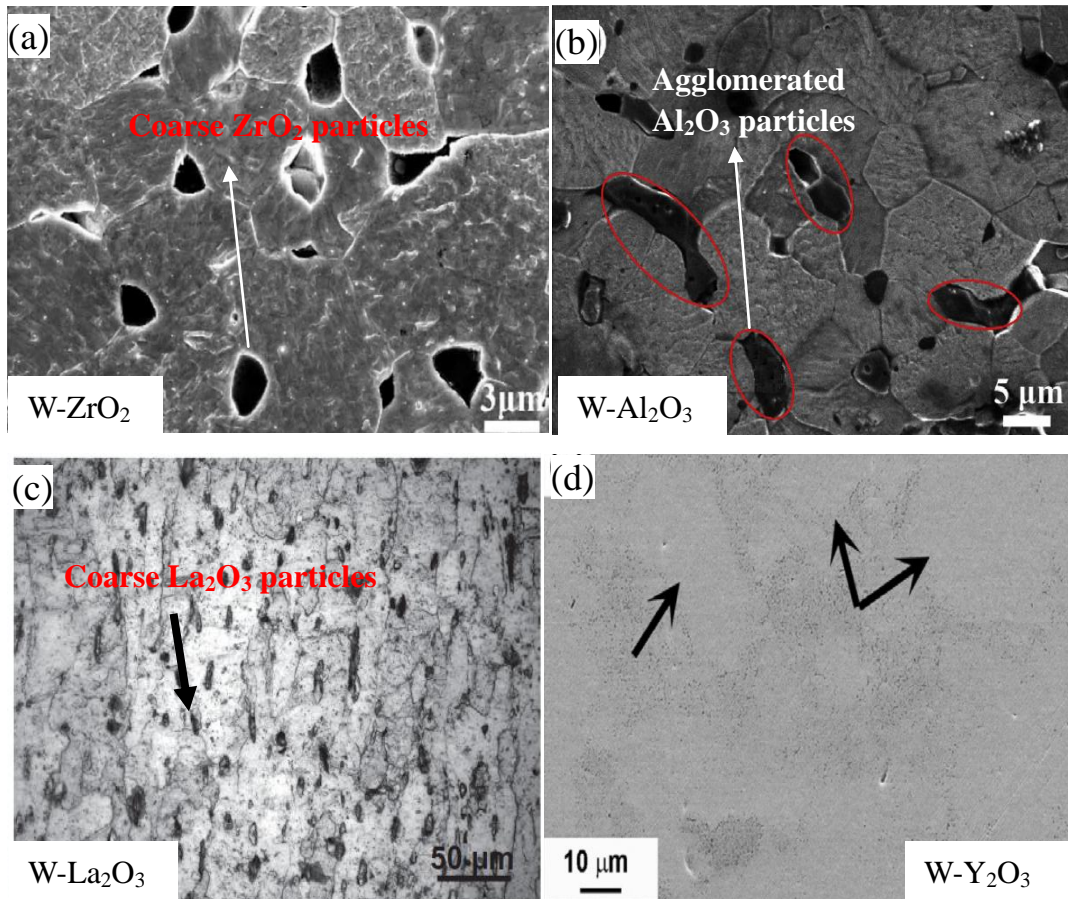
Fig.15. Microstructure of alloys reported in published references: (a, b) Powders prepared by a liquid-liquid method coupled with SPS process [61, 67], (c) Powders prepared by a liquid-solid doping method combined with sintering in vertical direction and hot swaging process [66] and (d) Powders prepared by a liquid-solid doping method couple with SPS process [12].

Table 5 Microstructure and mechanical properties of ODS-W alloys.

Doping process	Sintering Process	Alloy	W grain size (μm)	Oxide particle size (μm)	Density (g/cm^3)/ Relative density (%)	Microhardness /Hv	Refs.
L-B	SPS	W-6vol% Al$_2$O$_3$	3.64	>1.0	-/94.96	347.39	[37]
	SPS	W-2.5%ZrO$_2$	4.65	2.5	-/99.6	480	[61]
	VD	W-2.5%ZrO$_2$	40-80	1.5	-/98.7	-	[63]
L-S^{a*}	VD	W-La$_2$O$_3$	50	3	-	-	[66]
	SPS	W-0.9wt%La$_2$O$_3$	-	2	17.8/94	406	[11]
	SPS	W-1.0%Y$_2$O$_3$	2.3	Nanosize	17.5/92	423	[12]
S-S	HIP	W-1%La$_2$O$_3$	-	>5	18.9/90.6	-	[68]
	HIP	W-Ti-0.5%Y$_2$O$_3$	2-5	>1.5	-	-	[69]
	SPS	W-5%HfO$_2$	11.6	>5	-/94.5	440	[70]
Proposed process	SPS	W-0.5%Zr(Y)O$_2$	4.67	0.25	18.44/96.7	472	
	SPS^{b*}	W-0.5%Zr(Y)O$_2$	4.1	<0.1	18.56/97.3	495	
	HIP^{b*}	W-0.5%Zr(Y)O$_2$	5.6	0.41	18.29/95.9	467	
	HIP^{b*}	92.25W-4.9Ni-2.1Fe-0.75ZrO$_2$	15	0.15	17.49/99.48	442	

a* Using ammonium paratungstate (APT) as tungsten source;

b* Powders prepared by proposed novel process combined with mechanical alloying.

Based on the above analysis, doped tungsten powders were prepared combined with composite hydrothermal method and mechanical alloying process. Then, through SPS and HIP processes, respectively, W-ZrO$_2$ and 92.25W-4.9Ni-2.1Fe-0.75ZrO$_2$ alloys were fabricated as shown in Fig. 16 a), b) and c). Seen from the inset in Fig. 16 a), a lots of nanosized particles are evenly distributed into the tungsten matrix. In Fig. 16 b), it is obvious that a large number of white particles are found within tungsten

grains. Due to long sintering time process, these particles are larger than those in Fig. 16 a). The alloy corresponding to Fig. 16 c) and d), was produced by conventional sintering in hydrogen atmosphere, at 2400 °C for 4h, followed by hot isostatic pressing at 1400 °C for 1h under 250 MPa. Fig. 16 c) and d) shows its microstructure. Through BSE observation, the average size of the ZrO_2 particle is also about 400 nm, which is smaller than oxide particle in ODS-W alloy reported in those already published results. The microstructure and properties researches have be detailedly presented in latest study of F. N. Xiao and al. [71].
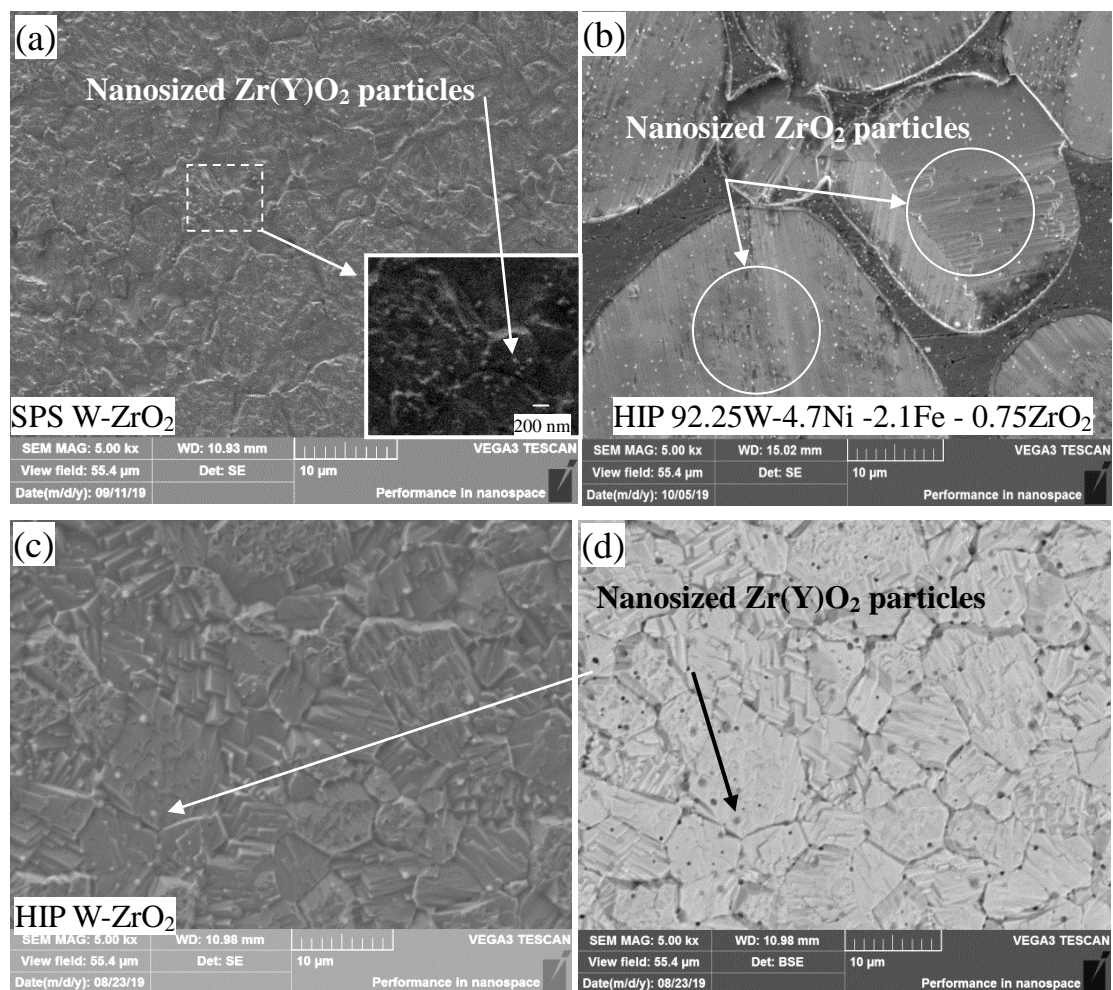
Fig. 16. Microstructure of alloys fabricated by different sintering process: (a) SPS process, (b) HIP sintering process, (c) HIP sintering process and (d) HIP sintering process (BSE image).

4. Conclusions

(1) Composite hydrothermal method and H_2 reduction process were used to synthesize W-Zr(Y)O_2 powders. The W-Zr(Y)O_2 powder particles are distinguishable and 75% of W-Zr(Y)O_2 powder particles are less than 3 μm in size;

(2) α-HATB was synthesized through hydrothermal reaction and the synthesis mechanism was investigated. This anoxic condition hinders the formation of m-WO_3, but promotes the occurrence of the β-HATB;

(4) After reduction at 900 °C for 2h, the obtained W- Zr(Y)O_2 powders have narrower size distribution with a mean particle size less than 2 μm. The distribution slope parameter (S_w) in range of 4~5, the reduced coefficient of uniformity (C_u) and span value (Ψ), indicate the narrower size distribution of W-Zr(Y)O_2 powders.

(5) Compared to the state of art, through SPS process, over 95% of particles in W-Zr(Y)O_2 alloy are less than 500 nm, which are smaller than those actually performs. The particles exhibit a good bonding with the tungsten phase. Additionnaly, through milling reduced powders, the Zr(Y)O_2 particle size further decrease. The nanosized particle dispersion strengthened W-Ni-Fe alloy can also be manufactured through HIP process.

Declaration of interest

There are no conflicts to declare.

Acknowledgements

Data availability

The raw/processed data required to reproduce these findings cannot be shared at this time as the data also forms part of an ongoing study.

Data will be presumably available for sharing before submission.

References

[1] J. Wang, G. Q. Zhao, L. Chen, J. L. Li, A comparative study of several constitutive models for powder metallurgy tungsten at elevated temperature, Mater. Des. 90 (2016) 91-100.

[2] Shizhong Wei, Liujie Xu. Review on Research Progress of Steel and Iron Wear-Resistant Materials. Acta Metall Sin, 2020, 56(4): 523-538.

[3] F. N. Xiao, Q. Miao, S. Z. Wei, Hydrothermal synthesis of nanoplates assembled hierarchical h-WO_3 microspheres and phase evolution in preparing cubic Zr (Y) O_2-doped tungsten powders, Adv. Powder Technol, 29 (2018) 2633-2643. https://doi.org/10.1016/j.apt.2018.07.011.

[4] Z.M. Xie, R. Liu, T. Zhang, Q.F. Fang, C.S. Liu, X. Liu, G.N. Luo, Achieving high strength/ductility in bulk W-Zr-Y_2O_3 alloy plate with hybrid microstructure, Mater. Des. 107 (2016) 144-152.

[5] A. A .E. Donoso, Computational study of the industrial synthesis of tungsten powders, Powder Technol, 344 (2019): 773-783. https://doi.org/10.1016/j.powtec.2018.12.065.

[6] R. Li, M. L. Qin, Z. Chen, S. J. Zhao , C. C. Liu, X. L. Wang, L. Zhang, J. D. Ma, X. H. Qu, Porous structure uniformity investigation of tungstenmatrix prepared by jet milled and annealed tungsten powder, Powder Technol, 339 (2018) 192–198. https://doi.org/10.1016/j.powtec.2018.08.021.

[7] Z. M. Wu, Y. X. Liang, E. G. Fu, J. L. Du, P. P. Wang, The process and mechanisms for the transformation of coarse grain to nanoscale grain in tungsten by ball milling, Powder Technol, 326 (2018): 222-227. https://doi.org/10.1016/j.powtec.2017.11.059.

[8] M. Asachi, E. Nourafkan, A. Hassanpour, A review of current techniques for the evaluation of powder mixing, Adv. Powder Technol, 29.7 (2018): 1525-1549. https://doi.org/10.1016/j.apt.2018.03.031.

[9] M. Staiger, P. Bowen, J. Ketterer, J. Bohonek, Particle size distribution

measurement and assessment of agglomeration of commercial nanosized ceramic particles, Journal of dispersion science and technology 23.5 (2002): 619-630.

[10] P. K. Senapati, B. K. Mishra, A. Parida, Modeling of viscosity for power plant ash slurry at higher concentrations: effect of solids volume fraction, particle size and hydrodynamic interactions, Powder Technol. 197, 2010, 1–8. https://doi.org/10.1016/j.powtec.2009.07.005

[11] M. A. Yar, S. Wahlberg, H. Bergqvist, Chemically produced nanostructured ODS-lanthanum oxide-tungsten composites sintered by spark plasma, J. Nucl. Mater, 408 (2011) 129-135. https://doi.org/10.1016/j.jnucmat.2010.10.060.

[12] M. A. Yar, S. Wahlberg, H. Bergqvist, Spark plasma sintering of tungsten-yttrium oxide composites from chemically synthesised nanopowders and microstructural characterization, J. Nucl. Mater. 412 (2011) 227-232. https://doi.org/10.1016/j.jnucmat.2011.03.007.

[13] B. Mamen, J. Song, T. Barriere, J. C. Gelin, Experimental and numerical analysis of the particle size effect on the densification behaviour of metal injection moulded tungsten parts during sintering, Powder. Techno. 270 (2015) 230-243. https://doi.org/10.1016/j.powtec.2014.10.019.

[14] G. J. Zhang, Y. J. Sun, R. M. Niu, J. Sun, J. F. Wei, B.H. Zhao, L.X. Yang, Microstructure and strengthening mechanism of oxide lanthanum dispersion strengthened molybdenum alloy, Adv. Eng. Mater. 6 (2004) 943-948. https://doi.org/10.1002/adem.200400072.

[15] Y. Hu, J. Wang, J. Ma, Effect of yttrium doping on the formation and stability of β-tungsten powder, Int. J. Refract. Met. Hard Mater. 72 (2018) 71-77. https://doi.org/10.1016/j.ijrmhm.2017.12.006.

[16] C. Lai, J. Wang, F. Zhou, Reduction, sintering and mechanical properties of rhenium - tungsten compounds, J. Alloy. Compd. 735(2018) 2685-2693. https://doi.org/10.1016/j.jallcom.2017.11.064.

[17] Y. T. Cui, J. S. Wang, W. Lui, X. Wang, Effect of scandia on tungsten oxide powder reduction process, J. Rare. Earth. 28 (2010) 202-205. https://doi.org/10.1016/s1002-0721(10)60274-8.

[18] F. N. Xiao, Q. Miao, S. Z. Wei, Z. Li, T. L. Sun, L. J. Xu, Microstructure and mechanical properties of W-ZrO$_2$ alloys by different preparation techniques, J Alloys Compd, 774 (2019): 210-221. https://doi.org/10.1016/j.jallcom.2018.09.321.

[19] Y. Han, J. Fan, T. Liu, The effect of trace nickel additive and ball milling treatment on the near-full densification behavior of ultrafine tungsten powder, Int. J. Refract. Met. Hard Mater. 34 (2012) 18-26. https://doi.org/10.1016/j.ijrmhm.2012.02.014.

[20] Z. Dong, N. Liu, Z. Ma, Synthesis of nanosized composite powders via a wet chemical process for sintering high performance W-Y$_2$O$_3$ alloy, Mater. Des. 69 (2017) 266-272. https://doi.org/10.1016/j.ijrmhm.2017.09.001.

[21] M. L. Zhao, L. M. Luo, J. S. Lin, X. Zan, X. Y. Zhu, G. N. Luo, Y. C. Wu, Thermal shock behavior of W-0.5 wt% Y$_2$O$_3$ alloy prepared via a novel chemical method, J. Nucl. Mater. 479 (2016) 616-622. https://doi.org/10.1016/j.jnucmat.2016.07.049.

[22] R. Liu, Z. Xie, Q. Fang, T. Zhang, X. Wang, T. Hao, C. Liu, Y. Dai, Nanostructured yttria dispersion-strengthened tungsten synthesised by sol-gel method, J. Alloy. Compd. 657 (2016) 73-80. https://doi.org/10.1016/j.jallcom.2015.10.059.

[23] H. Zhu, D. Tan, Y. Li, X. Yang, W. He, Refining mechanisms of arsenic in the hydrogen reduction process of tungsten oxide, Adv. Powder Technol. 26 (2015) 1013-1020. https://doi.org/10.1016/j.apt.2015.04.007.

[24] B. Liu, A. Shi, Q. Su, Recovery of tungsten carbides to prepare the ultrafine WC-Co composite powder by two-step reduction process, Mater. Des. 306 (2017) 113-119. https://doi.org/10.1016/j.powtec.2016.10.071.

[25] W. D. Schubert, E. Lassner, Production and characterization of hydrogen-reduced submicron tungsten powders. Part II: Controlled decomposition of APT and hydrogen reduction of the oxides, Int. J. Refract. Met. Hard Mater. 10 (1991) 171-183. https://doi.org/10.1016/0263-4368(91)90031-I.

[26] S. H. Hong, B. K. Kim, Fabrication of W–20 wt % Cu composite nanopowder and sintered alloy with high thermal conductivity, Mater. Lett, 57 (2003) 2761-2767. https://doi.org/10.1016/S0167-577X(03)00071-5.

[27] E. S. Yoon, J. S. Lee, S. T. Oh, B. K. Kim, Microstructure and sintering behavior of W–Cu nanocomposite powder produced by thermo-chemical process, Int. J. Refract. Met. Hard Mater. 20 (2002) 201-206. https://doi.org/10.1016/S0263-4368(02)00003-3.

[28] C. Wu, Preparation of ultrafine tungsten powders by in-situ hydrogen reduction of nano-needle violet tungsten oxide, Int. J. Refract. Met. Hard Mater. 29 (2011) 686-691. https://doi.org/10.1016/j.ijrmhm.2011.05.002.

[29] B. Zeiler, W. D. Schubert, B. Lux. On the reduction of NS-doped tungsten blue oxide-Part I: Literature review, Int. J. Refract. Met. Hard Mater, 10.2 (1991): 83-90. https://doi.org/10.1016/0263-4368(91)90026-K.

[30] X. W. Wu, J. S. Luo, B. Z. Lu, Crystal growth of tungsten during hydrogen reduction of tungsten oxide at high temperature, Trans. Nonferrous Met. Soc. China. 19 (2009) 785-789. https://doi.org/10.1016/S1003-6326(10)60152-5.

[31] C. Guo, S. Yin, Q. Dong, T. Sato, Simple route to $(NH_4)_x WO_3$ nanorods for near infrared absorption, Nanoscale 4.11 (2012): 3394-3398. https://doi.org/10.1039/c2nr30612c.

[32] I. Szilágyi, I. Sajó, P. Király, Phase transformations of ammonium tungsten bronzes, J. Therm. Anal. Calorim, 98.3 (2009): 707-716. https://doi.org/10.1007/s10973-009-0287-x.

[33] I. M. Szilágyi, F. Hange, J. Madarász, In situ HT- XRD Study on the Formation of Hexagonal Ammonium Tungsten Bronze by Partial Reduction of Ammonium Paratungstate Tetrahydrate, Eur. J. Inorg. Chem, 2006.17 (2006): 3413-3418. https://doi.org/10.1002/ejic.200500875.

[34] E. Lassner, W. D. Schubert, Tungsten: properties, chemistry, technology of the element, alloys, and chemical compounds, New York: Kluwer Academic/Plenum Publishers; 1999. https://doi.org/10.5860/choice.37-2788.

[35] L. Bartha, E. Lassner, W. D. Schubert, B. Lux, Special issue on the chemistry of non-sag tungsten, Int. J. Refract. Met. Hard Mater, 1995;13:1–164.

[36] C. P. Cui, Y. M. Gao, S. Z. Wei, G. S. Zhang, Y. C. Zhou, X. W. Zhu, Study on preparation and properties of molybdenum alloys reinforced by nano-sized ZrO_2

particles, Appl. Phys. A. 122 (2016) 214. https://doi.org/10.1007/s00339-016-9743-1.

[37] Wang C, Zhang L, Wei S, K.M. Pan, M. Aindow, Y. P. Yang, Microstructure and preparation of an ultra-fine-grained W-Al_2O_3 composite via hydrothermal synthesis and spark plasma sintering, Int. J. Refract. Met. Hard Mater, 72 (2018): 149-156. https://doi.org/10.1016/j.ijrmhm.2017.12.022.

[38] J. Q. Liao, B. Y. Huang, Particle size characterization of ultrafine tungsten powder, Int. J. Refract. Metals Hard Mater. 19 (2001) 89–99. https://doi.org/10.1016/S0263-4368(00)00051-2.

[39] R. Li, M. Qin, C. Liu, Z. Chen, X. Wang, X. Qu, Particle size distribution control and related properties improvements of tungsten powders by fluidized bed jet milling, Adv. Powder Technol. 28 (2017) 1603-1610. https://doi.org/10.1016/j.apt.2017.04.002.

[40] L. Z. L, J. Z. Zhao, Y. Wang, Y. L. Li, D. C. Ma, Y. Zhao, S. N. Hou, X. L. Hao, Oxalic acid mediated synthesis of WO_3-H_2O nanoplates and self-assembled nanoflowers under mild conditions, J. Solid. State. Chem. 184 (2011) 1661-1665. https://doi.org/10.1016/j.jssc.2011.05.008.

[41] M. Q. Xu, W. Zeng, F. Yang, L. Chen, Controllability of assemblage from WO3-H2O nanoplates to nanoflowers with the assistance of oxalic acid, J. Mater. Sci-Mater. El. 26 (2015) 6676-6682. https://doi.org/10.1007/s10854-015-3269-8.

[42] B. Miao , W. Zen, S. H. Hussain, Q. P. Mei, S. B. Xu, H. Zhang, Y. Q. Li, T. M. Li, Large scale hydrothermal synthesis of monodisperse hexagonal WO_3 Nanowire and the growth mechanism, Mater Lett. 147 (2015)12-15. https://doi.org/10.1016/j.matlet.2015.02.020.

[43] H. C. Yao, X. W. Wang, H. Dong, R. R. Pei, J. S. Wang, Z. J. Li, Synthesis and characteristics of nanocrystalline YSZ powder by polyethylene glycol assisted coprecipitation combined with azeotropic-distillation process and its electrical conductivity, Ceram. Int, 37.8 (2011): 3153-3160. https://doi.org/10.1016/j.ceramint.2011.05.055.

[44] G. Y. Guo, Y. L. Chen, W. J. Ying, Thermal, spectroscopic and X-ray diffractional analyses of zirconium hydroxides precipitated at low pH values, Mater.

Chem. Phys. 84 (2004) 308-314. https://doi.org/10.1016/j.matchemphys.2003.10.006.

[45] V. B. Glushkova, A. N. Lapshin, Specific features in the behavior of amorphous zirconium hydroxide: I. Sol-gel processes in the synthesis of zirconia, Glass. Phys. Chem. 29 (2003) 415-421. https://doi.org/10.1023/A:1025137313344.

[46] S. Cao, H. Chen, Nanorods assembled hierarchical urchin-like WO3 nanostructures: Hydrothermal synthesis, characterization, and their gas sensing properties, J. Alloy. Compd. 702 (2017) 644-648. https://doi.org/10.1016/j.jallcom.2017.01.232.

[47] J. H. Zhan, X. G. Yang, Y. Xie, B. F. Li, Y. T. Qain, Y. B. Jia, A solvothermal route for the synthesis of ammonium tungsten bronze, Solid State Ionics 126 (1999) 373-377. https://doi.org/10.1016/S0167-2738(99)00250-7.

[48] L. D. Clark, M. S. Whittingham, R. A. Huggins, An NMR Study of Ionic Motion in Ammonium Tungsten Bronze, J. Solid. State. Chem. 5 (1972) 487-493. https://doi.org/10.1016/0022-4596(72)90098-9.

[49] S. X. Cao, C. Zhao, T. Han, L.L. Peng, Hydrothermal synthesis, characterization and gas sensing properties of the WO_3 nanofibers, Mater Lett. 169 (2016) 17-20. https://doi.org/10.1016/j.matlet.2016.01.053.

[50] J. H. Ha, P. Muralidharan, D. K. Kim, Hydrothermal synthesis and characterization of self-assembled h-WO3 nanowires/nanorods using EDTA salts, J. Alloy. Compd. 475 (2009) 446-451. https://doi.org/10.1016/j.jallcom.2008.07.048.

[51] Y. Yu, W. Zeng, L. Yu, S. Wu, A novel $WO_3 \cdot H_2O$ nanostructure assembled with nanorods: Hydrothermal synthesis, growth and their gas sensing properties, Mater. Lett. 180 (2016) 51-54. https://doi.org/10.1016/j.matlet.2016.05.113.

[52] L. Huo, H. Zhao, F. Mauvy, F. Sébastien, L. Christine, P. Michel, J.C. Grenier, Synthesis and mixed conductivity of ammonium tungsten bronze with tunneling structures, Solid state Sci, 6.7 (2004): 679-688. https://doi.org/10.1016/j.solidstatesciences.2004.03.036.

[53] N. E. Fouad, A. K. H. Nohman, M. A. Mohamed, Characterization of ammonium tungsten bronze $[(NH_4)_{0.33} WO_3]$ in the thermal decomposition course of ammonium paratungstate, J. Anal. Appl. Pyrol, 56.1 (2000): 23-31.

https://doi.org/10.1016/S0165-2370(00)00084-X.

[54] I. M. Szila´gyi, J. Madara´sz, P. Kira´ly, G. Ta´rka´nyi, A. L. To´th, A. Szabo, Stability and controlled composition of hexagonal WO$_3$, Chem Mater. 2008; 20:4116–25. https://doi.org/10.1021/cm800668x.

[55] S. Cetinkaya , S. Eroglu, Reduction of tungsten trioxide with ethanol, Int. J. Refract. Met. Hard Mater, 64 (2017) 184–189. https://doi.org/10.1016/j.ijrmhm.2016.12.002.

[56] A. Kurlov, A. Gusev, Oxidation of tungsten carbide powders in air, Int. J. Refract. Met. Hard Mater, 41 (2013) 300-307. https://doi.org/10.1016/j.ijrmhm.2013.05.001.

[57] R.M. German and A. Bose, Injection Molding of Metals and Ceramics, 1997, Metal Powder Industries Federation, New Jersey.

[58] M. E. Sotomayor, A. Várez, B. Levenfeld, Influence of powder particle size distribution on rheological properties of 316 L powder injection moulding feedstocks, Powder Technology 200.1-2 (2010): 30-36. https://doi.org/10.1016/j.powtec.2010.02.003.

[59] F. Xiao, L. Xu, Y. Zhou, K. Pan, J. Li, W. Liu, S. Wei, A hybrid microstructure design strategy achieving W-ZrO$_2$(Y) alloy with high compressive strength and critical failure strain, J Alloy Compd. 708 (2017) 202-212. https://doi.org/10.1016/j.jallcom.2017.02.277.

[60] P. Bowen, Particle size distribution measurement from millimeters to nanometers and from rods to platelets, J. Disper. Sci. Technol, 23.5 (2002): 631-662.

[61] C. J. Wang, L. Q. Zhang, S. Z. Wei, K. M. Pan, X. C. Wu, Q. K. Li, Effect of ZrO2 content on microstructure and mechanical properties of W alloys fabricated by spark plasma sintering, Int. J. Refract. Met. Hard Mater. 79 (2019) 79-89.

[62] G. Liu, G. J. Zhang, F. Jiang, X. D. Ding, Y. J. Sun, J. Sun, E. Ma, Nanostructured high-strength molybdenum alloys with unprecedented tensile ductility, Nature Mater. 12 (2013) 344.

[63] Z. Li, L. J. Xu, S. Z. Wei, C. Chen, F. N. Xiao, Fabrication and mechanical properties of tungsten alloys reinforced with c-ZrO$_2$ particles, J. Alloy. Comp. 769 (2018) (2018) 694-705.

[64] C. J. Wang, L. Q. Zhang, S. Z. Wei, K. M. Pan, X. C. Wu, Q. K. Li, Preparation, microstructure, and constitutive equation of W-0.25 wt% Al_2O_3 alloy, Mater. Sci. Eng. A 744 (2019) 79-85.

[65] F. N. Xiao, L. J. Xu, Y. C. Zhou, K. M. Pan, J. W. Li, W. Liu, S. Z. Wei, Preparation, microstructure, and properties of tungsten alloys reinforced by ZrO_2 particles, Int. J. Refract. Met. Hard Mater. 64 (2017) 40-46.

[66] Y. Shen, Z. Xu, K. Cui, J. Yu, Microstructure of a commercial W-1% La2O3 alloy, J. Nucl. Mater. 455 (2014) 234-241.

[67] C. J. Wang, L. Q. Zhang, K. M. Pan, S. Z. Wei, X. C. Wu, Q. K. Li, Effect of Al_2O_3 content and swaging on microstructure and mechanical properties of Al_2O_3/W alloys, Int. J. Refract. Met. Hard Mater. 84 (2020) 105082.

[68] A. Muñoz, M. A. Monge, B. Savoini, M. E. Rabanal, G. Garces, R. Pareja, La_2O_3-reinforced W and W-V alloys produced by hot isostatic pressing, J. Nucl. Mater. 417 (2011) 508-511.

[69] R. Liu, Z. M. Xie, T. Zhang, Q. F. Fang, X. P. Wang, T. Hao, C. S . Liu, Y. Dai, Mechanical properties and microstructures of W-1% Y_2O_3 microalloyed with Zr, Mater. Sci. Eng. A 660 (2016) 19-23.

[70] Y. M. Ki, K. H. Lee, E. P. Kim, D. I. Cheong, S. H. Hong, Fabrication of high temperature oxides dispersion strengthened tungsten composites by spark plasma sintering process, Int. J. Refract. Met. Hard Mater. 27 (2009) 842-846.

[71] F. N. Xiao, Q. Miao, S. Z. Wei, T. Barriere, G. Cheng, S. W. Zuo, L. J. Xu, Uniform nanosized oxide particles dispersion strengthened tungsten alloy fabricated involving hydrothermal method and hot isostatic pressing, J Alloys Compd, 824 (2020): 153894. https://doi.org/10.1016/j.jallcom.2020.153894.